Single-Ion Spectroscopy of Two Electric Quadrupole Transitions in Ytterbium Ion and Excess Micromotion Minimization

Yasutaka IMAI

Electronic Science and Engineering
Kyoto University

2020

Abstract

The oscillator of which frequency is stabilized to an atomic transition is called the atomic clock. Recently, the lasers stabilized to the transitions in optical region, called optical clocks, have been developed. Uncertainties of the optical clocks referenced to transitions of long lifetimes in trapped single ions [1] or ensemble atoms in optical lattices [2] reach approximately 10^{-18}. This value is two orders magnitude better than that realized in best atomic clocks in microwave. The best uncertainty at this moment is realized using trapped single aluminum ions [1]. Considerable attention arises to the optical clocks of such low uncertainties from the application to experimental studies of the fundamental physics. Long-term comparison of frequency ratio of the optical clocks referenced to the transitions of different sensitivities to the variation of the fine structure constant α has been conducted to search for a temporal variation of α. Precise measurement of isotope shifts is proposed as a method for search for an unknown particle related with new physics beyond the standard model of the particle physics [3].

In this thesis, we have established the systems and techniques for single-ion spectroscopy of the ${}^2S_{1/2}-{}^2D_{3/2}$ and ${}^2S_{1/2}-{}^2D_{5/2}$ electric quadrupole transitions in Yb^+. ${}^{171}Yb^+$ has magnetic-field insensitive clock transitions of $m_F = 0-m_{F'} = 0$ with relatively simple hyperfine structures owing to the nuclear spin of 1/2. The ${}^2S_{1/2}-{}^2D_{3/2}$ transition in ${}^{171}Yb^+$ is involved in the list of the secondary representation of the second. Its uncertainty, reported to be the order of 10^{-16}, are potentially improved, as well as that of the ${}^2S_{1/2}-{}^2D_{5/2}$ transition. Improving the uncertainties of the two quadrupole transitions are essential in the search for a temporal variation of α using only ${}^{171}Yb^+$. The ${}^2S_{1/2}-{}^2F_{7/2}$ transition, to be compared, has a large sensitivity to α variation of which sign is opposite to those of the two quadrupole transitions and an optical clock referenced to the ${}^2S_{1/2}-{}^2F_{7/2}$ transition has been reported with a better uncertainty of 3×10^{-18} [4]. We could explore other effects of temporal variations by frequency ratio measurement of the two quadrupole transitions because the two have similar sensitivities to α

variation. Yb^+ has five stable even isotopes which have no hyperfine structures. The $^2S_{1/2} - {}^2D_{5/2}$ transition is suitable for precise measurements of the isotope shifts.

The feature of this study are as follows. (i) We developed a computer-controlled spectroscopy system for single Yb^+ ions. (ii) We established the techniques required for single-ion spectroscopy of the $^2S_{1/2} - {}^2D_{3/2}$ transition in $^{171}Yb^+$. Laser cooing and spectroscopy of $^{171}Yb^+$ are complicated because of the hyperfine structures. Unlike previous works, we prepared independent lasers to drive all transitions for closing laser-cooling cycle, and determined the experimental condition. (iii) We investigated the resolved-sideband spectra. The spectra are used for evaluation of the residual translational energy, which is a large factor of the uncertainty of the single-ion optical clock. We investigated the relation of the structures in the resolved-sideband spectra to the residual displacement of the time-averaged ion position from the trap center that simultaneously causes excess micromotions.

In Chapter 1, we describe the background of this study. Then, we clarify the purpose and features of this study in the development of the optical clock.

In Chapter 2, we introduce the theories and principles related with this thesis. We briefly describe the principles of RF trap and laser cooling. Then, we explain the excess micromotion. The micromotion is the motion driven by the RF voltage for trapping. Excess micromotions are induced by the displacement of the time-averaged ion position from the trap center caused. The displacement is caused by a stray DC electric field. Minimization of excess micromotion is inevitable to reduce the uncertainties caused by the translational energy of the trapped single ions. The detection methods for excess micromotions are briefly described. Finally, we summarize the properties of Yb^+.

In Chapter 3, we describe the experimental setup used in this thesis. Radiation at 370 nm used for laser cooling is generated via sum frequency mixing of two extended-cavity laser diodes (ECLD) at 822 nm and 671 nm. To maintain cooling of single Yb^+ ions for a long time, we stabilized the frequency of the cooling radiation based on the offset locking of the ECLD at 822 nm to the master laser in the clock laser system for the $^2S_{1/2} - {}^2D_{5/2}$ transition. The drift of sum frequency was reduced below 200 kHz/ h. This is sufficient for long-term laser cooling. Then, we constructed a computer-controlled high-speed spectroscopy system containing an FPGA with a small dead time. The precise frequency scanning using an offset locked laser or an external acousto-optic modulator was developed. The details of the RF traps used are also described.

In Chapter 4, we describe laser cooling of Yb^+ ions. First, we established the techniques required for laser cooling using $^{174}Yb^+$ ions which have no hyperfine structures. We controlled the number of the trapped ions using stepwise increase in the fluorescence intensity caused by one-by-one loading of Yb^+ ions into the trap. We minimized an excess micromotion along the cooling beam by detecting it using RF-photon correlation method. Second, laser cooling of $^{171}Yb^+$, which have hyperfine structures, was performed. We determined the power of the subcooling laser for driving of the $^2S_{1/2}(F=0)-{}^2P_{1/2}(F=1)$ transition to eliminate optical pumping in the $^2S_{1/2}(F=0)$ state. We investigated the optimal intensity and direction of the magnetic field for efficient cooling of the two isotopes to eliminate optical pumping in the magnetic sublevels.

In Chapter 5, we describe the single-ion spectroscopy of the $^2S_{1/2}-{}^2D_{5/2}$ transition in $^{174}Yb^+$. Yb^+ in the $^2D_{5/2}$ state decays to the $^2F_{7/2}$ state of a branching ratio of 80 %. Because of the extremely long lifetime of several years of the $^2F_{7/2}$ state, we easily detect the excitation to the $^2D_{5/2}$ state by observing the electron shelving in the $^2F_{7/2}$ state. To continue probing the $^2S_{1/2}-{}^2D_{5/2}$ transition, we depopulate $^{174}Yb^+$ ions from the $^2F_{7/2}$ state to the $^2S_{1/2}$ state by driving the $^2F_{7/2}-{}^1D[5/2]_{5/2}$ transition. We conducted single-ion spectroscopy of the $\Delta m_j = \pm 2$ transitions selected from ten Zeeman components by applying the magnetic field perpendicular to the polarization of the clock laser. Then, we resolved the $m_j = -1/2 - m_{j'} = -5/2$ transition in two $\Delta m_j = -2$ transitions by applying a sufficient large magnetic field. We observed the carrier and the resolved-sideband spectra of the transition caused by the secular motions of single $^{174}Yb^+$ ions.

In Chapter 6, we describe the single-ion spectroscopy of the $^2S_{1/2}-{}^2D_{3/2}$ transition in $^{171}Yb^+$. The hyperfine structure of $^{171}Yb^+$ complicates the procedure for the spectroscopy. We determined the parameters in each step of the spectroscopy. First, we measured that the power of the main repumping laser, with which the $^2D_{3/2}(F=1)-{}^3D[3/2]_{1/2}(F=0)$ is driven, is required to be smaller than 1 mW to decouple the $^2D_{3/2}(F=2)$ state from the cooling cycle by eliminating saturation broadening. Second, we adjusted the time required for pumping to the initial state of the spectroscopy of the $^2S_{1/2}(F=0,\, m_F=0)$ by blocking the subcooling laser. Subsequently, we conducted the spectroscopy of the $^2S_{1/2}(F=0)-{}^2D_{3/2}(F=2)$ transition. We improved the resolution from separating all Zeeman components of $\Delta m_F = 0, \pm 1, \pm 2$ transitions to observing the carrier and resolved-sideband spectra of the $m_F = 0 - m_{F'} = 0$ transition. By compensating the frequency drift of the clock laser, we obtained the spectral width of the carrier spectrum

to be 380 Hz. The width is approximately limited by the linewidth of the clock laser.

In Chapter 7, we describe detailed investigations of the resolved-sideband spectra of trapped single ions using the ${}^2S_{1/2}-{}^2D_{5/2}$ transition in ${}^{174}\mathrm{Yb}^+$. We found that the resolved-sideband spectra had structures of subsideband. From the measurement of the dependence of the RF electric resonance signal on the voltages applied for trapping, we revealed that the subsidebands were generated from mixing of the phase modulation by the secular motions in the different directions. The strong subsideband intensity indicates that the single ion was confined out of the Lamb-Dicke region. We three-dimensionally minimized excess micromotions by detecting them using RF-photon correlation in two different directions and the pseudopotential modulation. This resulted in great reduction of the subsidebands in the resolved-sideband spectra. This observation indicated that the heating rate was increased as the residual displacement of the time-averaged ion position from the trap center, which induced excess micromotions, was larger.

The progress made through this study will enables us to stabilize the clock laser frequency to the ${}^2S_{1/2}(F=0, m_F=0)-{}^2D_{3/2}(F'=2, m_{F'}=0)$ transition in ${}^{171}\mathrm{Yb}^+$ and evaluate the uncertainties in various factors of the frequency shifts towards realization of an single-ion optical clock. The optical clocks based on the ${}^2S_{1/2}(F=0, m_F=0)-{}^2D_{5/2}(F'=2, m_{F'}=0)$, and ${}^2S_{1/2}(F=0, m_F=0)-{}^2F_{7/2}(F'=3, m_{F'}=0)$ transitions are also feasible. Frequency ratio measurements among the three optical clocks will contribute to the redefinition of the second through the evaluation of their reproducibilities and to a more reliable search for a temporal variation of α.

Acknowledgement

The thesis was written based on the work at quantum optical engineering laboratory in Kyoto University, Japan. During my doctoral course, I was given much support from many people in various ways. Without their help, I could not have finished writing this thesis. I would like to express my appreciation to them here.

First of all, I would like to express my deepest gratitude to my supervisor Professor Hirofumi Yamada for giving me the opportunity to write this study as a thesis and being concerned about me.

I would like to show my greatest appreciation to Professor Yoichi Kawakami for his carefully considered feedback and valuable advises for my thesis despite his busyness.

I also greatly appreciate receiving guidance from Professor Osamu Sakai of Department of Electronic Systems Engineering, the University of Shiga. He led me earnestly as a supervisor until he left from Kyoto University.

I am deeply grateful to Associate Professor Kazuhiko Sugiyama whose practical assistance and suggestions were of inestimable value for my study. Without his help, this thesis doesn't complete.

I would like to offer my special thanks to Professor Masao Kitano whose enormous support and insightful comments were invaluable during my Ph.D. course.

I want to thank to Assistant Professor Toshihiro Nakanishi who provided technical help and sincere encouragement.

I also want to thank Professor Noboru Sasao and Professor Koji Yoshimura for supporting me after my graduation.

My special thanks go to Associate Professor Tomoyuki Uehara, Dr. Yugo Onoda, Associate Professor Yasuhiro Tamayama, Associate Professor Hirokazu Kobayashi, Mr. Shuichiro Noro, Assistant Professor Shuhei Tamate, Associate Professor Yosuke Nakata, Dr. Mitaki Masatoshi, Technical Official Shuhei hatanaka, Ph.D. Hiroto Fujisaki for their support and daily discussion in quantum optical engineering laboratory.

Contents

Abstract **i**

Acknowledgement **v**

1 Introduction **1**
1.1 Background 1
1.2 Ytterbium ion optical clock 3
1.3 Outline of thesis 6

2 Principle **9**
2.1 Paul trap 9
2.1.1 Excess micromotion 12
2.1.2 Anharmonicity 13
2.2 Laser cooling 13
2.3 Detection method of excess micromotion 17
2.3.1 RF-photon correlation method 17
2.3.2 Modulating pseudopotential method 18
2.4 Level structure of Yb^+ 19

3 Experimental setup **25**
3.1 Light sources 25
3.1.1 Cooling lasers 25
3.1.2 Repumping lasers 26
3.1.3 Clock lasers 28
3.1.4 Deexciting laser 30
3.1.5 Photoionizing lasers 30
3.2 RF Trap 32
3.3 Fluorescence detection 32
3.4 System for spectroscopy 34

4 Laser cooling of single Yb ion **39**
4.1 Laser cooling of $^{174}Yb^{+}$ 39
4.1.1 Loading of single $^{174}Yb^{+}$ ions 39
4.1.2 Adjustment of magnetic field 41
4.1.3 Micromotion minimization using RF-photon correlation detection 41
4.2 Laser cooling of $^{171}Yb^{+}$ 43
4.2.1 Adjustment of magnetic field 43

5 Single-ion spectroscopy of $^{2}S_{1/2}-{}^{2}D_{5/2}$ clock transition in $^{174}Yb^{+}$ 47
5.1 Interrogation sequence of the $^{2}S_{1/2}-{}^{2}D_{5/2}$ transition 47
5.2 Zeeman components and resolved-sideband spectra of $^{2}S_{1/2}-{}^{2}D_{5/2}$ transition 48

6 Single-ion spectroscopy of $^{2}S_{1/2}-{}^{2}D_{3/2}$ clock transition in $^{171}Yb^{+}$ 55
6.1 Preparation for spectroscopy: decoupling $^{2}D_{3/2}(F=2)$ state from cooling cycle 55
6.2 Procedure of spectroscopy of $^{2}S_{1/2}-{}^{2}D_{3/2}$ transition 56
6.3 Spectra of $^{2}S_{1/2}(F=0)-{}^{2}D_{3/2}(F'=2)$ transition 59
6.3.1 Zeeman components and resolved-sideband 59
6.3.2 Carrier spectrum of $m_F=0-m_{F'}=0$ component . . . 59

7 Resolved-sideband spectra and minimization of excess micromotions 67
7.1 Resolved-sideband spectra with one-directional micromotion minimization 68
7.2 Micromotion minimization in three dimensions 73
7.3 Discussions 78

8 Conclusions 85
8.1 Conclusions 85
8.2 Prospect 88

List of Publications 94
A Full Length Papers with Review 95
B Conference Proceedings 95
C International Conferences with Review 95

Chapter 1

Introduction

1.1 Background

The oscillator of which frequency is stabilized to an atomic transition is called the atomic clock. Some atomic clocks have extremely low uncertainties. Uncertainties of the atomic clocks referenced to the transition between the hyperfine structure in the ground state of caesium atom in microwave region reach the order of 10^{-16} [5]. The frequency of this transition is used for one of the seven defining constants of the International System of Unit (SI). Recently, the lasers stabilized to the transitions in optical region, called optical clocks, have been developed [1, 4, 6, 7]. The fractional instability of the atomic clock is evaluated in terms of the Allan variance $\sigma_y^2(\tau)$. The root of Allan variance is inversely proportional to the quality factor and signal-to-noise ratio of the reference transition. When the noise is a white frequency noise, $\sigma_y(\tau)$ is expressed in [8],

$$\sigma_y(\tau) \propto \frac{1}{Q}\frac{1}{\sqrt{N}}\sqrt{\frac{1}{M}} = \frac{\Delta\nu}{\nu_0}\frac{1}{\sqrt{N}}\sqrt{\frac{T}{\tau}}, \tag{1.1}$$

where N is the number of the atoms, $Q = \nu_0/\Delta\nu$ is the quality factor of the reference transition given by the transition frequency ν_0 and the linewidth of the transition $\Delta\nu$, $M = T/\tau$ is the number of the measurements given by the measurement duration T and the total measurement duration τ. The optical frequency is 10^4 times higher than the microwave transition frequency in caesium atom. Therefore, the optical clock is an attractive to improve the uncertainty of the frequency standard. Uncertainties of approximately

10^{-18} have been reported in the optical clocks referenced to transitions of long lifetimes in cold atoms or ions in vacuum [1, 2, 4]. Two methods have been realized for providing the reference transition of such low uncertainties; one is trapped single ions, and the other is ensemble atoms in optical lattices. The former, the single-ion clock is based on single ions confined using electromagnetic field [9]. Although use of only single ion limits the frequency stability owing to the worst signal-to-noise ratio, the single-ion clocks have good uncertainties. So far, the best uncertainty at this moment of 9.7×10^{-19} has been reported in an aluminum ion clock [1]. The latter, the optical lattice clock is based on ensemble atoms in periodic potentials produced by interference of lasers [2]. Because approximately 1000 atoms trapped in the lattice can be used, optical lattice clocks realize better frequency stabilities. A large factor of uncertainty of light shifts caused by the light field of the optical lattice has been reduced by introducing the concept of the magic wavelength of the optical lattice, where the light shifts to the upper and lower states of the clock transition are the same.

Such low uncertainties are attractive for application to experimental studies of the fundamental physics. One of the applications of the optical clocks is to search for a temporal variation of the fine structure constant α. Variations in the fundamental constants is possible in the theories that unify the gravitation to the other three fundamental interactions [10]. The search is conducted by observing the differential variation in two clock transitions of different sensitivities to variation of α. The frequency of the electronic transition f_{E} can be described as

$$f_{\mathrm{E}} = CR_{\infty}cF(\alpha), \tag{1.2}$$

where C is a numerical constant, R_{∞} is the Rydberg constant, c is the speed of light, and $F(\alpha)$ is a dimensionless function of α. The temporal variation of f_{E} can be written as

$$\frac{\partial f_{\mathrm{E}}}{\partial t} = \frac{\partial \ln(R_{\infty}c)}{\partial t} + A\frac{\partial \ln \alpha}{\partial t}, \tag{1.3}$$

where A is the sensitivity to variation of α, which can be described as

$$A = \frac{\partial \ln F(\alpha)}{\partial \ln \alpha}. \tag{1.4}$$

The value of A depends on transitions. A possible temporal variation of the Rydberg constant would be a common value in all of transitions. Consequently, we can observe a temporal variation of α by measurement of frequency ratio between different optical transitions as [11, 12]

$$\frac{\partial\left(f_{\mathrm{E1}}/f_{\mathrm{E2}}\right)}{\partial t} = (A_1 - A_2)\frac{\partial \ln \alpha}{\partial t}. \tag{1.5}$$

The sensitivity A of each transition used as a reference in the optical clock is listed in Table 1.1 [13]. Recently, precise measurement of isotope shifts is proposed as a method for search for an unknown particle related with new physics beyond the standard model of the particle physics [3].

1.2 Ytterbium ion optical clock

Singly ionized ytterbium (Yb^+) is one of the candidates which provides reference clock transitions used for optical clocks. Yb^+ has alkalimetal-like level structure. It has strong transitions which can be used for Doppler cooling, and weak transitions of long lifetimes for the reference of a clock. An advantage of Yb^+ is that 171 isotope has a nuclear spin I of 1/2. The odd isotopes of atoms having alkalimetal-like level structure possess $m_F = 0 - m_{F'} = 0$ transitions which are insensitive to 1st-order Zeeman effect in low magnetic fields. Owing to $I = 1/2$, $^{171}Yb^+$ has relatively simple hyperfine structures and magnetic sublevels.

Yb^+ has three clock transitions in the blue and violet region: the $^2S_{1/2} - {}^2F_{7/2}$ electric octupole transition, and the $^2S_{1/2} - {}^2D_{3/2}$ and the $^2S_{1/2} - {}^2D_{5/2}$ electric quadrupole transitions. The $^2S_{1/2} - {}^2F_{7/2}$ and $^2S_{1/2} - {}^2D_{3/2}$ transitions are involved in the list of the secondary representation of the second. The $^2S_{1/2} - {}^2F_{7/2}$ transition has an extremely long lifetime of several years [14]. An uncertainty of 3×10^{-18} is demonstrated using the $^2S_{1/2} - {}^2F_{7/2}$ transition as a reference of an optical clock [4].

For the $^2S_{1/2} - {}^2D_{3/2}$ transition, the present uncertainty of the order of 10^{-16} [15] can be potentially improved, as an optical clock referenced against the quadrupole transition in strontium ion has an uncertainty of 1.2×10^{-17} [16]. Note that the $^2D_{3/2}$ state is included in the laser cooling cycle in even isotopes of Yb^+ that have no hyperfine structures. In $^{171}Yb^+$, the $^2D_{3/2}(F = 2)$ state is decoupled from the cooling cycle and the $^2S_{1/2}(F = 0) - {}^2D_{3/2}(F = 2)$ transition is used for the clock transition. Therefore, techniques for decou-

Atom	Transition	Sensitivity A
H	$^1S_{1/2} - {}^2S_{1/2}$	2.4×10^{-5}
Ca	$^1S_0 - {}^3P_0$	0.016
Sr	$^1S_0 - {}^3P_0$	0.06
Yb	$^1S_0 - {}^3P_0$	0.31
Hg	$^1S_0 - {}^3P_0$	0.81

Ion	Transition	Sensitivity A
Al^+	$^1S_0 - {}^3P_0$	0.008
In^+	$^1S_0 - {}^3P_0$	0.18
Ca^+	$^2S_{1/2} - {}^2D_{5/2}$	0.15
Sr^+	$^2S_{1/2} - {}^2D_{5/2}$	0.43
Ba^+	$^2S_{1/2} - {}^2D_{3/2}$	2.5
	$^2S_{1/2} - {}^2D_{5/2}$	2.4
Yb^+	$^2S_{1/2} - {}^2D_{3/2}$	1.00
	$^2S_{1/2} - {}^2D_{5/2}$	1.03
	$^2S_{1/2} - {}^2F_{7/2}$	-6.0
Hg^+	$^2S_{1/2} - {}^2D_{3/2}$	-1.5
	$^2S_{1/2} - {}^2D_{5/2}$	-2.9

Table 1.1: Sensitivity to variation of fine structure constant α.

Isotopes	Nuclear spin	Natural abundance
168	0	0.00123(3)
170	0	0.02982(39)
171	1/2	0.1409(14)
172	0	0.2168(13)
173	5/2	0.16103(63)
174	0	0.32026(80)
176	0	0.12996(83)

Table 1.2: Nuclear spin and natural abundance of stable isotopes of ytterbium.

pling and transition detection are required. Pioneering work on this topic has been conducted in [17, 18].

The $^2S_{1/2}-^2D_{5/2}$ transition is less attractive for the use for the reference in an optical clock owing to a shorter lifetime. The uncertainty of 2×10^{10} was reported in 1999 [19]. If we could increase the averaging time longer, however, $^2S_{1/2}-^2D_{5/2}$ transition would have a similar potential in uncertainty to the $^2S_{1/2}-^2D_{3/2}$ transition. In addition, the $^2S_{1/2}-^2D_{5/2}$ transition is easily detected in even isotopes using the decay to the $^2F_{7/2}$ state with a branching ratio of 80 %.

These transitions are useful for the application to the fundamental physics. The $^2S_{1/2}-^2F_{7/2}$ transition has a large sensitivity to variation of α. As listed in Table 1.1, its sensitivity is the largest in the clock transitions which have been so far used in optical clocks [20]. The $^2S_{1/2}-^2D_{3/2}$ and $^2S_{1/2}-^2D_{5/2}$ transitions have sensitivity signs that are opposite to that of the $^2S_{1/2}-^2F_{7/2}$ transition. Therefore, we can search for a temporal variation of α using only Yb^+. This simplifies the experimental setup and removes common-mode frequency fluctuations and shifts such as the gravitational red shift by using the same single Yb^+ ion in the same trap. The $^2S_{1/2}-^2D_{3/2}$ and $^2S_{1/2}-^2D_{5/2}$ transitions have similar sensitivities to α [20]. This enables us to examine other effects that cause temporal variations.

Yb^+ has five stable even isotopes, and therefore is suitable for precise measurement of isotope shifts. The natural abundance of the stable isotopes and the nuclear spin quantum number of Yb are listed in Table 1.2. The $^2S_{1/2}-^2D_{5/2}$ transition is easily detected in even isotopes. This is a target transition used for precise measurement of isotope shifts. From the application not only to the optical clocks but also to the fundamental physics raised above, improvement of the uncertainties of optical clocks referenced to the two quadrupole transitions is essential.

1.3 Outline of thesis

In this study, we have established the systems and the techniques for single-ion spectroscopy of the $^2S_{1/2}-^2D_{3/2}$ and $^2S_{1/2}-^2D_{5/2}$ electric quadrupole transitions in Yb^+. The features of this study are as follows. (i) We developed a computer-controlled fast spectroscopy system for the two quadrupole transitions in single Yb^+ ions. (ii) We established the techniques required for conducting single-ion spectroscopy of the $^2S_{1/2}(F=0)-^2D_{3/2}(F=2)$ transition in $^{171}Yb^+$. (iii) We conducted detailed investigations of the resolved

motional-sideband spectra.

For (i), to measure the excitation probability, we need to repeat the excitation trial considerable number of times because we can only know whether the excitation succeeds or not from one excitation trial to a single ion. Therefore, to detect spectra of single ions, we developed a fast measurement system including a digital delay generator configured by employing a field programmable gate array (FPGA) containing a processor (National Instruments myRIO).

For (ii), as described in Section 1.2, owing to the hyperfine structures, the technologies are required for faster cooling and single-ion spectroscopy of the transition: eliminating and completing optical pumping to the $^2S_{1/2}(F = 0)$ state for laser cooling and initialization in the spectroscopy procedure, respectively, and decoupling the $^2D_{3/2}(F = 2)$ state from the cooling cycle. Unlike previous works, we prepared independent lasers to drive all transitions used for laser cooling of $^{171}Yb^+$. We determined the conditions required for the spectroscopy from the detailed measurements.

For (iii), the resolved motional-sideband spectra is important because they are used for evaluation of the translational energy of the trapped single ions, which is a large factor for the uncertainty. We found that the resolved-sideband spectra had subsideband structures. We investigated the origin of the structures and the effect of the displacement from the trap center of the time-averaged position of a single ion on the structures through minimization of excess micromotions.

In Chpater 2, we describe the theories and principles required for understanding this thesis.

In Chapter 3, we present the experimental setup. To cool the trapped Yb^+ ions for a long periods of time, we improved the frequency stability of the cooling radiation based on offset locking of one of the ECLD used for sum-frequency mixing generating the cooling radiation to the master laser in the clock laser system for the $^2S_{1/2} - ^2D_{5/2}$ transition.

In Chapter 4, we describe laser cooling of Yb^+ ions. First, we established the techniques for laser cooling of $^{174}Yb^+$ which has no hyperfine structures, including a method for loading single ions. Then, we laser cooled $^{171}Yb^+$ by eliminating the optical pumping in the hyperfine structure in the $^2S_{1/2}$ ground state.

In Chapter 5, we describe the single-ion spectroscopy of the $^2S_{1/2} - ^2D_{5/2}$ transition in $^{174}Yb^+$. To conduct spectroscopy, we developed the spectroscopy system with a small dead time. We separated $\Delta m_F = \pm 2$ Zeeman components from all Zeeman components of $\Delta m_F = 0, \pm 1, \pm 2$ transitions.

Then, we probed $m_j = -1/2 - m_{j'} = -5/2$ transition and observed the carrier and resolved motional-sidebands spectra.

In Chapter 6, we describe the single-ion spectroscopy of the ${}^2S_{1/2} - {}^2D_{3/2}$ transition in ${}^{171}\mathrm{Yb}^+$. First, we determined the parameters in each step of the spectroscopy using our system. Subsequently, we conducted the spectroscopy improving the resolution from separating all Zeeman components of $\Delta m_F = 0, \pm 1, \pm 2$ transitions, to detecting the carrier and resolved motional-sidebands of the $m_F = 0 - m_{F'} = 0$ magnetic-field insensitive transition. Finally, we probed the carrier spectrum of the $m_F = 0 - m_{F'} = 0$ transition with higher resolution with compensating of the drift of the clock laser.

In Chapter 7, we describe the detailed investigation of the resolved motional-sideband spectra using the ${}^2S_{1/2} - {}^2D_{5/2}$ transition in ${}^{174}\mathrm{Yb}^+$. We revealed that the subsideband structures in the resolved-sideband spectra were caused by mixing of the phase modulation induced by the secular motions in the different directions, when the single ions were confined out of the Lamb-Dicke region. We developed three dimensionally minimization of excess micromotions detecting them by combination of RF-photon cross correlation using two different directions cooling beams and modulation of the pseudopotential depth. This simultaneously resulted in reducing the structures in the resolved motional-sideband spectra and cooled the secular motions close to the Doppler cooling limit.

In Chapter 8, we conclude this study including future plans.

Chapter 2

Principle

In this chapter, we describe the theories and principles required for understanding this study.

Long interaction time and localization of atoms in small space are essential for exploring or using properties of atoms. The ions confined using electromagnetic field are suitable for such proposes. We describe the principle of the Paul or RF trap used for confinement ions in Section 2.1. In the practical experiments, excess micromotions are almost always encountered [21] and they increase the translational energy of trapped ions. In Section 2.1, we also summarize this problem. In Section 2.2, we describe the principle of laser cooling used for reducing the translational energy of trapped ions. As described in Chapter 1, we chose Yb^+ as an ion to investigate towards realization of optical clocks. We describe the properties of Yb^+ including level structures and lifetimes of the levels.

2.1 Paul trap

According to the consequence of Laplace equation, potential generated by only static electric field cannot form a potential minimum point. However, time averaged potential minimum point can be realized by an alternating electric field as was proposed by W. Paul [22].

Arrangement of Paul trap is shown in Fig. 2.1. When a single ion is confined in a quadrupole potential that has a reflection symmetry in xy-plane and a rotational symmetry around z-axis, the potential, generated by applying an electric voltage that $V_0 = V_{\mathrm{DC}} + V_{\mathrm{AC}} \cos \Omega t$ between two endcap and a ring electrodes, is described in cylindrical coordinates in the form

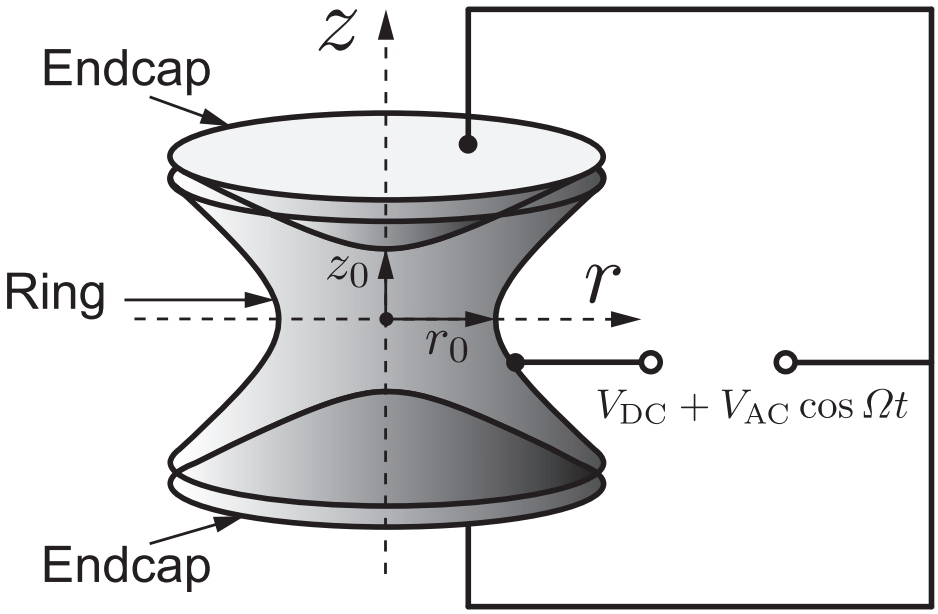

Figure 2.1: Arrangement of Paul trap. The inner surfaces of electrodes are hyperboloids described as $r^2 + z^2 = r_0^2$. The radius of ring electrode r_0 and the half distance between endcap electrodes have the ratio of $r_0/z_0 = \sqrt{2}$.

$r^2 = x^2 + y^2$ as

$$\phi(r, z, t) = (V_{\mathrm{DC}} + V_{\mathrm{AC}} \cos \Omega t) \frac{r^2 - 2z^2}{r_0^2 + 2z_0^2}, \tag{2.1}$$

where V_{AC} and Ω are the amplitude and the angular frequency of an AC driving voltage, respectively; V_{DC} is the DC voltage used for adjusting the ratio of the potential depths in the radial and axial directions; $2r_0$ is the inner diameter of the ring electrode; $2z_0$ is the minimum distance between endcap electrodes. Typically, the radial and axial distances exhibits the relation $r_0^2 = 2z_0^2$.

The motion of a single ion of mass m and a charge Q in the potential given by Eq. (2.1) is expressed by the Mathieu equation:

$$\ddot{u}_i + (a_i + 2q_i \cos \Omega t) \frac{\Omega^2}{4} u_i = 0 \qquad (i = r, z), \tag{2.2}$$

where the parameter a_i and q_i are defined as

$$a_z = -2a_r = -\frac{8QV_{\mathrm{DC}}}{mr_0^2\Omega^2}, \tag{2.3}$$

$$q_z = -2q_r = -\frac{4QV_{\mathrm{AC}}}{mr_0^2\Omega^2}. \tag{2.4}$$

When $|a_i| \ll 1$ and $|q_i| \ll 1$, the first order solution to Eq. (2.2) is given by

$$u_i \sim u_{1,i} \cos(\omega_i t + \phi_i) \left(1 + \frac{q_i}{2} \cos \Omega t\right), \tag{2.5}$$

with

$$\omega_i = \frac{\Omega}{2} \sqrt{a_i + \frac{q_i^2}{2}}, \tag{2.6}$$

where ϕ_i is the phase determined by the initial condition. The harmonic motion of an amplitude $u_{1,i}$ and an angular frequency ω_i is called the secular

motion.

2.1.1 Excess micromotion

In the practical setup, a stray DC field $E_{\mathrm{s},i}$ exists. This modifies the equation of motion and the first-order solution given by Eqs. (2.2) and (2.5), respectively as [21]

$$\ddot{u_i} + (a_i + 2q_i \cos \Omega t)\frac{\Omega^2}{4} u_i = \frac{QE_{\mathrm{s},i}}{m}, \tag{2.7}$$

and

$$u_i(t) \sim [u_{0,i} + u_{1,i} \cos(\omega_i t + \phi_i)] \left(1 + \frac{q_i}{2} \cos \Omega t\right), \tag{2.8}$$

respectively, where

$$u_{0,i} \sim \frac{4QE_{\mathrm{s},i}}{m\left(a_i + \frac{q_i^2}{2}\right)\Omega^2} \sim \frac{QE_{\mathrm{s},i}}{m\omega_i^2}. \tag{2.9}$$

The displacement $u_{0,i}$ caused by the stray field $E_{\mathrm{s},i}$ induces an excess micromotion of an amplitude $\frac{1}{2}u_{0,i}q_i$. The kinetic energy of the ion averaged over a period of the secular motion is given by [21]

$$\langle E_{k,i} \rangle \simeq \frac{1}{2} m \langle \dot{u}_i^2 \rangle = \frac{1}{4} m u_{1,i}^2 \left(\omega_i^2 + \frac{1}{8} q_i^2 \Omega^2\right) + \frac{m q_i^2 u_{0,i}^2 \Omega^2}{16}. \tag{2.10}$$

The first term is the averaged energy owing to the secular motion, while the second term is the one contributed by excess micromotion. The excess micromotion cannot be efficiently laser cooled because the motion is always driven by the trap AC voltage. Therefore, minimization of the excess micromotion by compensation of the stray electric DC field is necessary. A phase difference in the AC driving voltage applied to the electrodes is another cause of the excess micromotion [21]. We will discuss the detection methods for the excess micromotion in Section 2.3.

2.1.2 Anharmonicity

The actual trap potential has a small deviation from the ideal harmonic potential. The trap electrodes typically have a reflection symmetry in the xy-plane. The leading anharmonicity is a small octupole potential, *i.e.*, [23, 24]

$$\Delta V = \frac{1}{2} V_0 C_4 \left(\frac{1}{r_0^4} \right) (z^4 - 3z^2 r^3 + \frac{3}{8} r^4). \tag{2.11}$$

This potential induces higher harmonics of secular frequencies and couples the radial and axial secular motions [25]. Note that the anharmonicity increases with the distance from the trap center as excess micromotions do.

2.2 Laser cooling

The ions trapped in a RF trap are typically thermalized to a temperature of several thousand Kelvin. When the confinement of the ions in Lamb-Dicke region of optical wavelength is required, we must reduce the translational energy of the trapped ions, and laser cooling is used [26]. In this section, we describe the theory of laser cooling.

Laser cooling is performed using radiation pressure generated from interaction between the ion and cooling-laser beam. For simplicity, we assume a two-level ion, which has a resonance frequency of ω_0, in the one-dimensional harmonic potential without micromotion. The ion motions at velocity of $\boldsymbol{v} = v\cos(\omega t)\boldsymbol{x}$ in cooling beam field with a wavevector $\boldsymbol{k_L} = k_L \boldsymbol{x}$ traveling along the direction of the ion's motion. The photon absorption from the cooling beam gives the ion the momentum $\Delta p = \hbar k_L$ in the beam-propagation direction, while the spontaneous emission from upper level transfers no momentum on average because the spontaneous emission is isotropic. Therefore the ion is accelerated when the ion moves along the propagation direction of the cooling beam, and is deaccelerated when the ion moves against the propagation direction. If the laser frequency ω_L is detuned lower than ω_0, the absorption probability increases when the ion velocity and the beam propagation direction are opposite, and it decreases when they are the same because of the Doppler shift $-\boldsymbol{k_L} \cdot \boldsymbol{v}$ as shown in Fig. 2.2. It is called Doppler cooling.

We will discuss the cooling rate and the cooling limit quantitatively. If the spontaneous decay rate of the upper state Γ is much faster than motion

frequency of the ion ($\Gamma \gg \omega$), the ion's position and velocity can be regarded as constant during a cycle of photon absorption and spontaneous emission. In this case of what is called weak-binding limit, we can consider that the ion receives radiation pressure averaged over many cycles of photon absorption and spontaneous emission. The averaged radiation pressure is given by [27]

$$F_a = \left(\frac{dp}{dt}\right) = \hbar k_{\mathrm{L}} \Gamma \rho, \tag{2.12}$$

where ρ is the probability of the ion in upper state

$$\rho = \frac{s_0/2}{1 + s_0 + 4(\Delta_{\mathrm{L}} - \boldsymbol{k_{\mathrm{L}}} \cdot \boldsymbol{v})^2/\Gamma^2}, \tag{2.13}$$

$s_0 = 2\Omega_{\mathrm{R}}^2/\Gamma^2$ is the saturation parameter at the resonance composed of Rabi frequency Ω_{R}, $\Delta_{\mathrm{L}} = \omega_{\mathrm{L}} - \omega_0$ is the laser detuning. When the ion's velocity v is small so that the Doppler shift $-\boldsymbol{k_{\mathrm{L}}} \cdot \boldsymbol{v}$ is smaller than the laser detuning Δ_{L} and the decay rate Γ, Eq. (2.12) can be expanded in v as

$$F_a \simeq F_0(1 - \beta v), \tag{2.14}$$

where F_0 and β are

$$F_0 = \hbar k_{\mathrm{L}} \Gamma \frac{s_0/2}{1 + s_0 + 4(\Delta_{\mathrm{L}}/\Gamma)^2}, \tag{2.15}$$

$$\beta = -\frac{8k\Delta_{\mathrm{L}}/\Gamma^2}{1 + s_0 + 4(\Delta_{\mathrm{L}}/\Gamma)^2}. \tag{2.16}$$

In the condition of $\Delta_{\mathrm{L}} < 0$, β works as friction coefficient that provide viscous drag for the ion. Because the averaged velocity of the ion in harmonic potential $\langle v \rangle$ is 0, the cooling rate is given by

$$\frac{dE_{\mathrm{cool}}}{dt} = \langle F_a v \rangle = F_0(\langle v \rangle - \beta \langle v^2 \rangle) = -\beta F_0 \langle v^2 \rangle. \tag{2.17}$$

The final temperature reached by Doppler cooling is limited by the photon-recoil energy which the ion receives when photon absorption and spontaneous

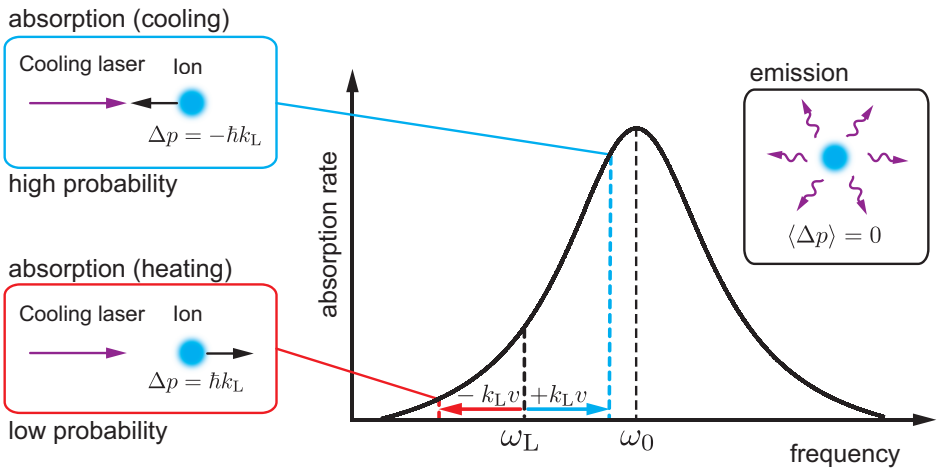

Figure 2.2: Process of Doppler cooling.

emission occur. From conservation momentum and energy of the ion and the photon, the recoil energy from an absorbed photon R_{abs} and that from an emitted photon R_{emi} are described as

$$R_{\mathrm{abs}} = \frac{(\hbar|\boldsymbol{k}_{\mathbf{L}}|)^2}{2m}, \tag{2.18}$$

$$R_{\mathrm{emi}} = \frac{(\hbar|\boldsymbol{k}_{\mathbf{emi}}|)^2}{2m}, \tag{2.19}$$

where $|\boldsymbol{k}_{\mathbf{emi}}| = \omega_{\mathrm{emi}}/c$, and m is mass of the ion. Because the photon absorption and spontaneous emission occur in different geometry, we define scaling factor ξ due to the angular pattern of the spontaneous emission. Then, the heating rate is described as

$$\frac{dE_{\mathrm{heat}}}{dt} = (R_{\mathrm{abs}} + R_{\mathrm{emi}})\Gamma\rho = \frac{(\hbar k_{\mathrm{L}})^2}{2m}(1+\xi)\Gamma\rho, \tag{2.20}$$

The final temperature can be expressed by the equilibrium between the cooling rate and the heating rate from Eqs. (2.17) and (2.20)

$$\frac{1}{2}m\langle v^2\rangle = \frac{1}{2}k_{\mathrm{B}}T = -\frac{\hbar\Gamma}{16}(1+\xi)\left\{(1+s_0)\frac{\Gamma}{2\Delta_{\mathrm{L}}} + \frac{2\Delta_{\mathrm{L}}}{\Gamma}\right\}. \tag{2.21}$$

For $\Delta_{\mathrm{L}} = -\sqrt{1+s_0}\,\Gamma/2$, the temperature achieves minimal value as

$$T_{\mathrm{min}} = \frac{\hbar\Gamma\sqrt{1+s_0}}{4k_{\mathrm{B}}}(1+\xi), \tag{2.22}$$

where k_{B} is the Boltzmann constant. The temperature in the limit of $s_0 \to 0$ is called as Doppler cooling limit.

In the case of Yb^+, the ${}^2S_{1/2} - {}^2P_{1/2}$ transition, of which spontaneous decay rate is $\Gamma/2\pi = 19.6\,\mathrm{MHz}$, is used for laser cooling described in Section 2.4. For the isotropic photon emission ($\xi = 1/3$), the Doppler cooling limit of the transition is about 0.31 mK.

2.3 Detection method of excess micromotion

To minimize the excess micromotion, high sensitive detection methods for the excess micromotions is inevitable. The RF-photon correlation method [21,28, 29], modulating the psuedopotential [18, 21], and parametric resonance [30] are widely used. The sensitivities of these methods have been extensively discussed [21, 29]. We use a RF-photon correlation method and modulation of the pseudopotential as we will describe later. The former detects a Doppler shift to a cooling beam caused by the micromotion. Because the cooling laser is detuned lower than the resonance frequency, the excitation rate changes with the Doppler shift. The latter modulates the restoring force. This results in a modulation in the time-averaged ion position when a stray DC field exists.

2.3.1 RF-photon correlation method

From Eq. (2.8), the velocity of the ion owing to the excess micromotion is given by

$$v_{\mathrm{micro},i}(t) = -\frac{1}{2}u_{0,i}q_i\Omega\sin(\Omega t). \tag{2.23}$$

The velocity induces the Doppler shift to the cooling laser frequency ω_{L} as,

$$-\boldsymbol{k}_{\mathbf{L}}\cdot\boldsymbol{v}_{\mathbf{micro}} = \beta\Omega\sin(\Omega t), \tag{2.24}$$

where

$$\beta = \frac{1}{2}\sum_{i=r,z} k_{\mathrm{L},i}u_{0,i}q_i. \tag{2.25}$$

For simplicity, we assume that the Doppler shift is much smaller than the spontaneous decay rate ($|\beta\Omega| \ll \Gamma$) and the intensity of the laser is sufficiently weak to ignore saturation. Then, the detected fluorescence rate is described as

$$R = R_{\max}\frac{(\Gamma/2)^2}{(\Gamma/2)^2 + (\Delta_{\mathrm{L}} - \beta\Omega\sin(\Omega t)^2}, \tag{2.26}$$

where $R_{\max}$ is the maximum fluorescence rate detected using the laser. If the laser frequency is detuned to be $\Delta_{\mathrm{L}} = -\Gamma/2$, Eq. (2.26) can be simplified as

$$R \simeq R_{\max}\left(\frac{1}{2} + \frac{\beta\Omega}{\Gamma}\sin(\Omega t)\right). \tag{2.27}$$

More detailed investigation including the saturation is developed in [29], where the maximum sensitivity is not obtained as $\Delta_{\mathrm{L}} = -\Gamma/2$. As shown in the Eq. (2.27), the fluorescence of the ion induced by the cooling laser is modulated by the excess micromotion. Therefore, the excess micromotion can be detected using correlation between the fluorescence rate and phase of the trap AC voltage, which is called RF-photon correlation method. The practical sequence of the method is described in later Section 4.1.3. Note that the method is insensitive to excess micromotion in the direction perpendicular to the beam propagation $\boldsymbol{k}_{\mathbf{L}}$. For minimization excess micromotion in insensitive direction, the other beam irradiated along different direction from first one or other methods that are sensitive to the excess micromotion perpendicular to the beam are required.

2.3.2 Modulating pseudopotential method

According to Eq. (2.9), displacement of the ion due to the excess micromotion is inversely proportional to the depth of pseudopotential. We consider the ion located in the center of the cooling laser beam, which has a Gaussian intensity profile given by

$$I(x) = I_0 \exp\left(\frac{-2x^2}{w_0^2}\right). \tag{2.28}$$

For simplicity, we assume that V_{DC} is 0 V and the modulation of the trap RF amplitude ΔV_{AC} is small as $\Delta V_{\mathrm{AC}}/V_{\mathrm{AC}} \ll 1$. When the modulation of the trap RF amplitude is applied at frequency $\omega_{\mathrm{mod}} \ll \Omega$, variation of the displacement is described as

$$\Delta u_{0,i} \simeq 2u_{0,i}\frac{\Delta V_{\mathrm{AC}}}{V_{\mathrm{AC}}}\cos\omega_{\mathrm{mod}}t. \tag{2.29}$$

Here, we define the $\boldsymbol{d}$ as the unit vector perpendicular to the propagation of the beam $\boldsymbol{k_L}$. The maximum variation of the beam intensity which the ion receives is described as

$$\Delta I_{\max} = I_0 \exp\left(\frac{-2(\boldsymbol{\Delta u_0} \cdot \boldsymbol{d})^2}{w_0^2}\right). \tag{2.30}$$

When we ignore saturation of the transition, maximum variation of the fluorescence $\Delta R_{\max}$ is given by

$$\frac{\Delta R_{\max}}{R_{\max}} = \frac{\Delta I_{\max}}{I_0}. \tag{2.31}$$

Therefore, the excess micromotion can also be detected as the fluorescence variation caused by the modulation of trap AC voltage. Note that, unlike the RF-photon correlation method, this method is sensitive to the excess micromotion in the direction perpendicular to the beam propagation.

2.4 Level structure of Yb^+

Yb has the atomic number of 70 and belongs to the lanthanoid atoms included in the rare earth element. Yb does not react with water at room temperature, and hardly oxidizes. The natural abundance and the nuclear spin number of the seven stable isotopes are already shown in Table 1.2. The features and the current status of optical clocks referenced to the three clock transitions, *i.e.*, the ${}^2S_{1/2} - {}^2F_{7/2}$, ${}^2S_{1/2} - {}^2D_{3/2}$, and ${}^2S_{1/2} - {}^2D_{5/2}$ transitions in Yb^+, and their application to experimental exploration in the field of fundamental physics are discussed in Section 1.2. The transitions and their lifetimes related with this study are shown in Table 2.1.

The energy level structure of ${}^{174}Yb^+$ relevant to this thesis is shown in Fig. 2.3. The ${}^2S_{1/2} - {}^2P_{1/2}$ transition at 370 nm is driven for Doppler cooling and detection of the ion. To end the cooling cycle, the ${}^2D_{3/2}$ state is deexcited to the ground state by driving the ${}^2D_{3/2} - {}^3D[3/2]_{1/2}$ transition at 935 nm [35]. We observe spectra with resolved motional sidebands by driving the ${}^2S_{1/2} - {}^2D_{5/2}$ quadrupole transition at 411 nm in single ${}^{174}Yb^+$ ions [33]. Yb^+ in the ${}^2D_{5/2}$ state has a lifetime of 7 ms [36] and decays to the ${}^2F_{7/2}$ state, of which lifetime of several years [14] with a branching ratio of 80 % [33]. Therefore, we detect the excitation to the ${}^2D_{5/2}$ state by observing the electron shelving in

State	Lifetime	Reference
$^2P_{1/2}$	8.10(13) ns	[31]
$^2D_{3/2}$	52.15(100) ms	[32]
$^2D_{5/2}$	7.2(3) ms	[33]
$^3D[3/2]_{1/2}$	37.7(5) ns	[34]
$^1D[5/2]_{5/2}$	< 160 ms	[19]
$^2F_{7/2}$	≤ 10 year	[14]

Table 2.1: Lifetimes of the states in Yb^+.

the $^2F_{7/2}$ state. To continue probing the quadrupole transition, we deexcite $^{174}Yb^+$ ions from the $^2F_{7/2}$ state to the ground state by driving the $^2F_{7/2}-{}^1D[5/2]_{5/2}$ transition at 638 nm [33].

$^{171}Yb^+$, which is suitable for optical clock, has hyperfine structures. The partial term scheme of $^{171}Yb^+$ related with this study is shown Fig 2.4. The cooling and repumping transitions are the same as those for $^{174}Yb^+$, *i.e.*, $^2S_{1/2}-{}^2P_{1/2}$ and $^2D_{3/2}-{}^3D[3/2]_{1/2}$ transition, respectively. Although $^{171}Yb^+$ has the hyperfine structures, it has a cycling transition for laser cooloing *i.e.*, the $^2S_{1/2}(F=1)-{}^2P_{1/2}(F'=0)$ and the $^2D_{3/2}(F=1)-{}^3D[3/2]_{1/2}(F'=0)$ transitions. This is an advantage in only the atoms having $I=1/2$ among the atoms having alkari-metal-like level scheme. However, pumping to the $^2S_{1/2}(F=0)$ or $^2D_{3/2}(F=2)$ state is possible via off-resonant excitation of the transitions to the other hyperfine levels.

To deplete those hyperfine levels, we simultaneously drive the $^2S_{1/2}(F=0)-{}^2P_{1/2}(F'=1)$ and $^2D_{3/2}(F=2)-{}^3D[3/2]_{1/2}(F'=1)$ transitions as the sub-cooling and sub-repumping transitions, respectively, with independent light sources. Previously, depletion of the $^2S_{1/2}(F=0)$ state was conducted via frequency switching of an extended-cavity laser diode (ECLD) [17], modulation of the injection current of a LD [18], a second-order sideband generated using an electrooptic modulator (EOM) [37,38], or microwave-radiation-induced driving of the $^2S_{1/2}(F=0)-{}^2P_{1/2}(F'=1)$ transition [19, 39].

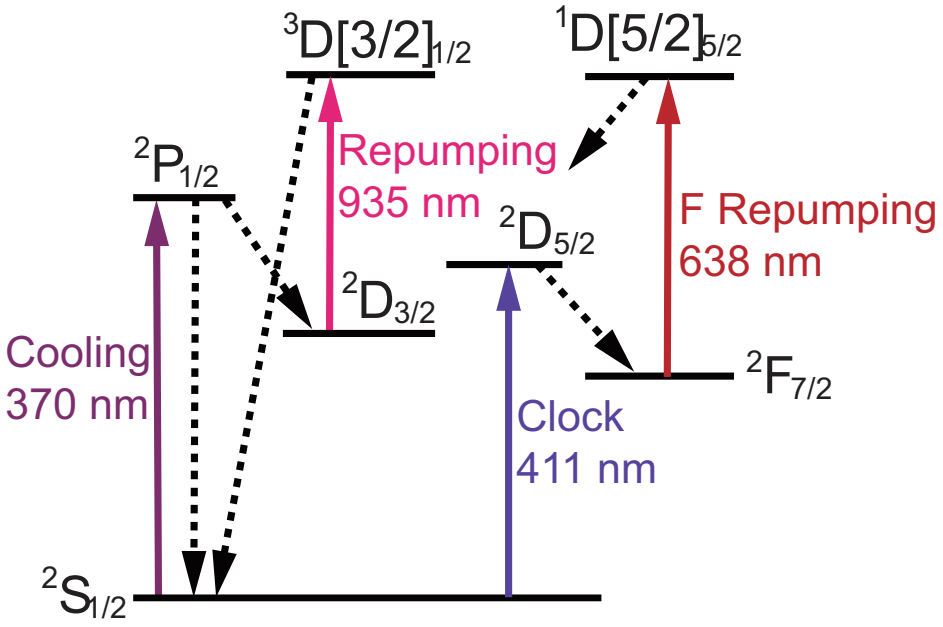

Figure 2.3: Partial term scheme of even isotope of Yb^+.

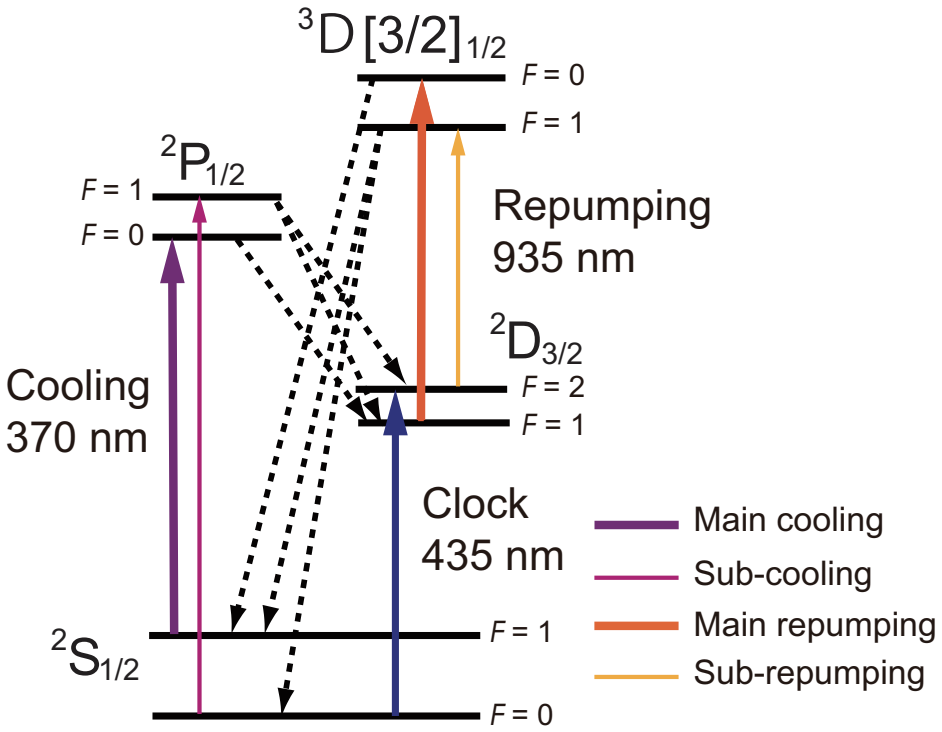

Figure 2.4: Partial term scheme of $^{171}Yb^+$. The relevant hyperfine splittings are as follows: $\Delta^2S_{1/2} = 12.6\,\mathrm{GHz}$, $\Delta^2P_{1/2} = 2.1\,\mathrm{GHz}$, $\Delta^2D_{3/2} = 0.86\,\mathrm{GHz}$, and $\Delta^3D[3/2]_{1/2} = 2.5\,\mathrm{GHz}$ [17].

Chapter 3

Experimental setup

In this chapter, we describe the experimental setup *i.e.*, light sources for laser cooling and spectroscopy of the clock transitions, RF traps and the systems to conduct laser cooling and single-ion spectroscopy.

3.1 Light sources

All lasers used in spectroscopy system of Yb^+ are produced from diode lasers. The 399 nm and 392 nm radiations are used for photoionization. The 370 nm and 935 nm radiations are employed for laser cooling. The 411 nm and 435 nm radiations are used for probe of the clock transitions. The 638 nm radiation is used for deexcitaion from $^2F_{7/2}$ to the ground state. The properties of lasers are summarized in the following sections.

3.1.1 Cooling lasers

The 370 nm radiation is generated via sum frequency mixing (SFM) of radiation from two extended-cavity laser diodes (ECLDs) at 822 and 671 nm using a power build-up cavity that resonates the two wavelengths [40]. The schematic of this cooling laser system is shown in Fig. 3.1. The ECLD frequency at 822 nm is stabilized to the resonance of a temperature-controlled reference cavity, the length of which is adjusted using a piezoelectric transducer (PZT). Then, the resonance of the power build-up cavity is locked to the stabilized frequency of the ECLD at 822 nm using a PZT. Finally, the ECLD frequency at 671 nm is locked to the resonance of the power build-up cavity using a PZT. The stability of the sum frequency is, therefore, limited by that of the ECLD at 822 nm. Its slow frequency drift is removed

through offset locking to the master laser in the clock laser system for the $^2S_{1/2} - {}^2D_{5/2}$ transitions, to cool the $^{171}Yb^+$ for a long period of time. The master laser is linenarrowed to a resonance of a high-finesse cavity. We will describe this later in detail. The drift of the master laser has been measured to be 20 kHz/ h. When the 822 nm ECLD for SFM is offset locked, its frequency fluctuation of the relative to the high-finesse-cavity-stabilized ECLD is smaller than 100 kHz at an averaging time of 0.1 s, corresponding to a sum-frequency fluctuation of less than 200 kHz. The sum frequency is roughly tuned to the main cooling transition of $^{174}Yb^+$ or $^{171}Yb^+$, respectively, by observing the absorption spectra of Yb^+ in a hollow-cathode lamp (Hamamatsu L2783). Further, the sum frequency is fine tuned by changing the offset frequency as we observe the fluorescence rate of the Yb^+ ions.

The sub-cooling radiation required for laser cooling of $^{171}Yb^+$ is generated from an ECLD at 370 nm. The diode chip is operated at 18.5 °C to tune the frequency to the sub-cooling transition. The base-plate temperature, on which the components of the ECLD are fixed, is controlled at 20 °C to maintain single-frequency operation around the sub-cooling transition for a long period of time. Continuous frequency tuning through adjustment of the ECLD cavity length using a PZT can only be achieved over a range of 1 GHz, because the chip does not have a special antireflection coating on the output facet. We sweep the injection current in a synchronous manner with a scan of the ECLD frequency using the PZT. This results in continuous frequency tuning up to 10 GHz. The ECLD frequency is adjusted by observing the absorption spectra of Yb^+ in a hollow-cathode lamp. Note that a similar ultraviolet ECLD has been reported in [41].

3.1.2 Repumping lasers

The main and sub-repumping radiation is generated from ECLDs at 935 nm. Each ECLD frequency is stabilized to the resonance of an independently prepared temperature-controlled reference cavity. The wavelengths of the main and sub-repumping lasers are tuned using a wavemeter with an uncertainty of 1×10^{-6} (Bureleigh WA1500). Their frequencies are fine tuned by observing the fluorescence rate of the Yb^+ ions.

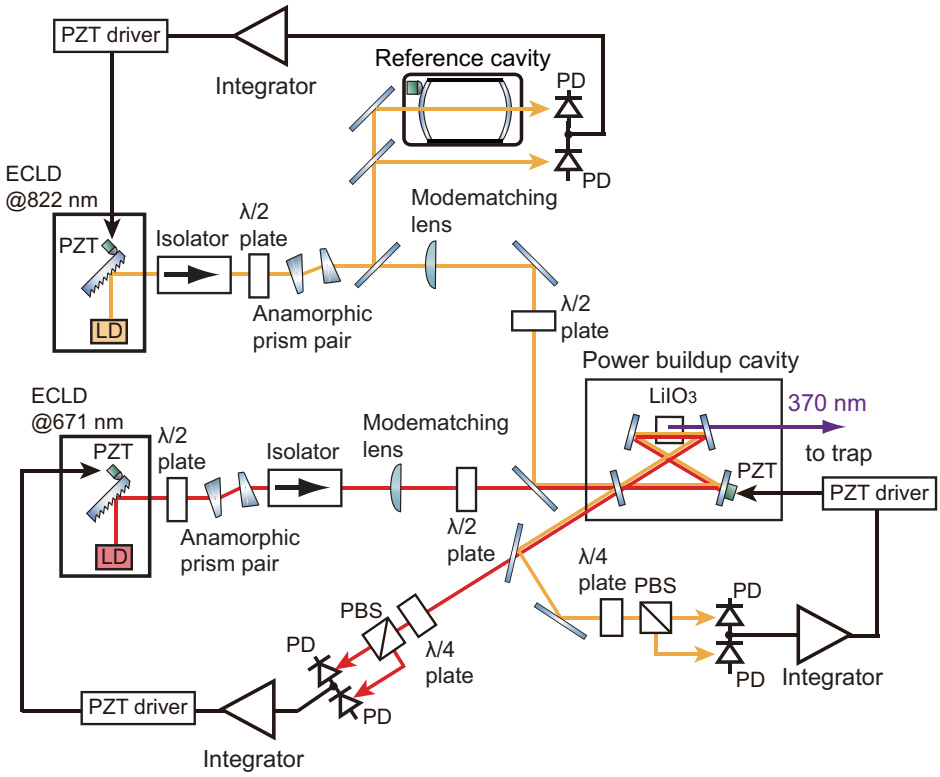

Figure 3.1: Main cooling laser system generated via SFM of radiation from ECLDs at 822 and 671 nm.

3.1.3 Clock lasers

System for $^2S_{1/2} - ^2D_{5/2}$ transition

A schematic diagram of the clock laser system for driving the $^2S_{1/2} - ^2D_{5/2}$ transition is shown in Fig. 3.2.

The clock laser system is composed of three stages, *i.e.*, a master laser linenarrowed to a resonance of a high-finesse cavity, slave laser phase-locked to the master laser with a variable offset frequency for frequency scanning, and second-harmonic generator [42]. Two ECLDs at 822 nm are used for the master and slave lasers. The master laser has a prenarrowing stage. First, the ECLD is fast frequency stabilized to a side of the resonance of the confocal cavity, which has a full-width at half maximum(FWHM) of the resonance and a free-spectral range(FSR) of 15 MHz and 2 GHz, respectively, using the injection current of the LD and a piezoelectric transducer (PZT) controlling the cavity length of the ECLD. This prenarrowing is aimed at maximizing the power concentration to the carrier and narrowing the carrier to be smaller than the resonance width of the high-finesse cavity. The measured prelinenarrowed linewidth is 10 kHz. Subsequently, the prelinenarrowed master laser is further linenarrowed to a resonance of the high-finesse cavity using FM sideband technique [**?**]. The high-finesse cavity, made of ultra-low thermal expansion glass, has a finesse and a FSR are 25000 and 2 GHz, respectively, and is placed in a temperature-controlled vacuum chamber. The fast fluctuation is feedback controlled using an acousto-optic modulator (AOM) connected externally to the ECLD. The slow fluctuation is feedback controlled using a PZT that controls the cavity length of the confocal cavity used in the pre-linenarrowing. The linewidth of the master laser is narrower than 500 Hz from the beat between two similar clock laser systems.

The beat between the linenarrowed master and the slave lasers is mixed down with a reference from a RF synthesizer using a double-balanced mixer. The injection current and the PZT adjusting the extended-cavity length of the slave laser are controlled to phase lock the beat to the reference. We frequency sweep the slave laser by changing the reference frequency. The second harmonic of radiation from the slave laser is generated using 10-mm-long β-BaB_2O_4 crystal placed in a power build-up cavity. We generate radiation at 411 nm of 1.6 mW from a cavity input power of 70 mW.

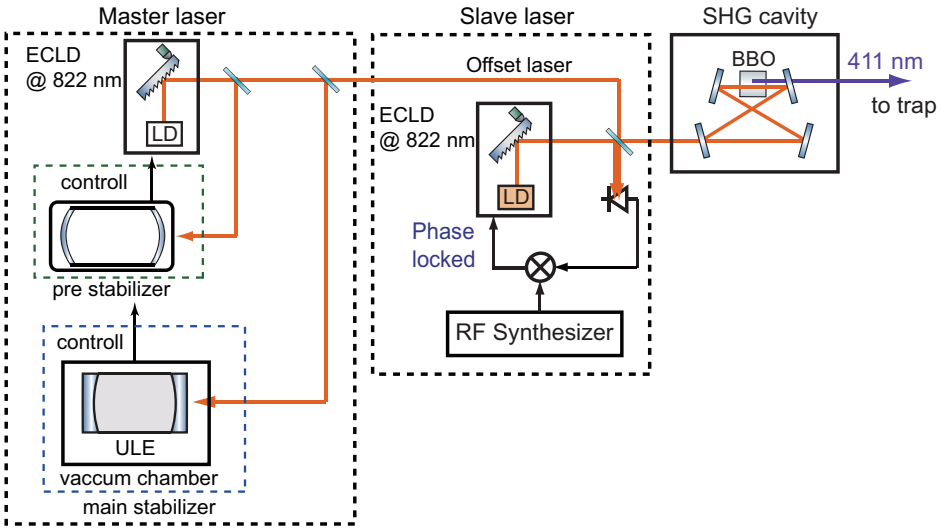

Figure 3.2: Schematic diagram of clock laser to drive ${}^2S_{1/2} - {}^2D_{5/2}$ transition. EOM: electrooptic modulator; FR: 45° Faraday rotator; PS: phase shifter.

System for $^2S_{1/2} - {}^2D_{3/2}$ transition

A schematic diagram of the clock laser system for driving the $^2S_{1/2} - {}^2D_{3/2}$ transition is shown in Fig. 3.3. An ECLD at 871 nm is linenarrowed to the resonance of a high-finesse cavity, using the FM sideband technique [43]. The high-finesse cavity is simultaneously used to linenarrow the clock laser at 822 nm, which is also referenced for frequency stabilization of the main cooling radiation as described above. We do not use an offset laser for frequency scanning in this clock laser system at 871 nm. Instead, the frequency scanning of the clock laser is conducted using a double-pass acoustooptic modulator (AOM). The driving frequency is generated from a synthesizer (Agilent E8663D) referenced to a Global Positioning System (GPS) clock, and is fed to the AOM after being amplified for maximum diffraction. Then, the second harmonic is generated using a 5 mm long $KNbO_3$ crystal placed in a power build-up cavity with a fundamental enhancement factor of 72. A maximum second harmonic power of 300 μW is generated from a fundamental power of 5.5 mW. We expect the linewidth of the clock radiation at 871 nm to be 500 Hz as we evaluated the linewidth of the master laser in the clock laser system at 822 nm described above.

3.1.4 Deexciting laser

The deexciting laser used for clearing out the ion in the $^2F_{7/2}$ metastable state to the $^2S_{1/2}$ ground state is generated from ECLD at 638 nm. The laser frequency is stabilized to the reference confocal cavity, of which the temperature is sensed by AD590 and controlled by heater. The wavelength is measured using the wavemeter as well as the repumping laser, and tuned not to appear the quantum jumps in cooling fluorescence signal caused by the ion pumped to the $^2F_{7/2}$ state while the clock laser for $^2S_{1/2} - {}^2D_{5/2}$ transition is irradiated.

3.1.5 Photoionizing lasers

Yb^+ ions are loaded through photoionization of neutral Yb atoms inside the trap [44]. The photoionization is conducted via two-step photoionization of Yb atoms. Driving of the $^1S_0 - {}^1P_1$ transition at 399 nm is the first step; this is followed by excitation from the $^1P_1$ beyond the ionization potential using radiation with a wavelength shorter than 394 nm. We use an ECLD at 399 nm and a LD at 392 nm for the first and second excitations, respectively. The

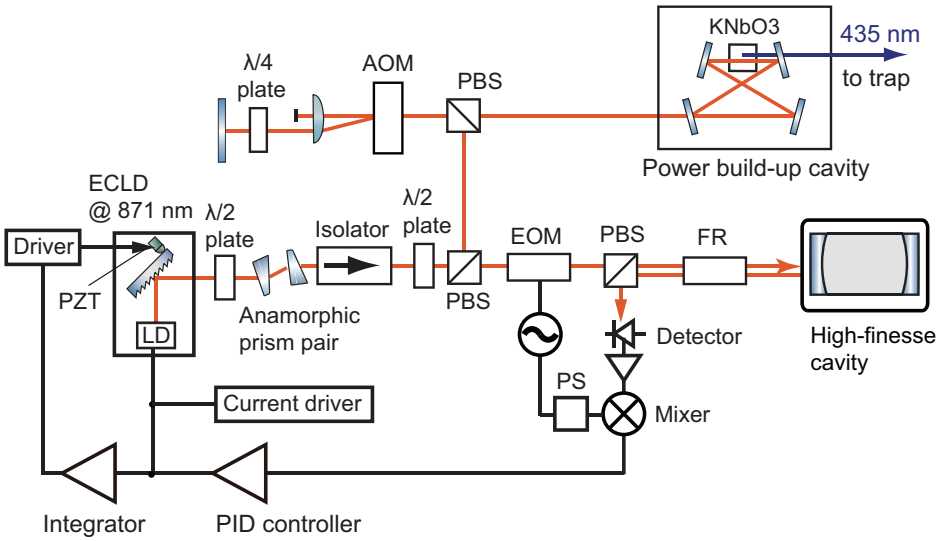

Figure 3.3: Schematic diagram of clock laser to drive ${}^2S_{1/2}(F = 0)$–${}^2D_{3/2}(F = 2)$ transition. EOM: electrooptic modulator; FR: 45° Faraday rotator; PS: phase shifter.

ECLD frequency for the first excitation is tuned by observing the absorption signal of the Yb atoms in a hollow-cathode lamp.

3.2 RF Trap

We use two identical RF traps of a conical cut [45] as $2r_0 = 0.8\,\mathrm{mm}$. We call one used for single-ion spectroscopy of $^{171}\mathrm{Yb}^+$ trap1, the other used for investigation of micromotion minimization trap2. RF driving voltages of $\Omega/2\pi = 13.25\,\mathrm{MHz}$ and $14.135\,\mathrm{MHz}$ for trap1 and trap2, respectively, and are applied between the ring and the endcap electrodes. Using helical resonators having quality factors of 250. The amplitude of the RF voltages are the same $V_{\mathrm{AC}} = 100\,\mathrm{V}$ in the two RF traps.

The compensation of the stray DC field is realized in the same manner for the two RF traps to minimize excess micromotions. To compensate the stray DC field in the axial direction, a DC voltage is applied to one of the endcap electrodes. For compensation in the radial direction, we introduce two pairs of compensation electrodes. Each pair of the compensation electrodes is composed of two wires: one is placed between the ring and one of the endcap electrodes, and the other between the ring and the other endcap in the same azimuthal angle to the rotational symmetry axis of the trap. Both pairs of compensation electrodes are fixed approximately at right angle to each other. We apply the same DC voltage to each pair of the compensation electrodes to minimize changes in the axial compensation voltage. Three pairs of coils are placed to cancel the environmental magnetic field and to apply a magnetic field in an arbitrary direction and strength.

Yb atoms are generated from an oven composed of a tantalum tube heated by a passing current. Small flakes of isotope-171-enriched or isotope-174-enriched metal are filled in two independent ovens. Yb^+ ions are loaded individually, and the step-wise increase in the fluorescence rate is observed, as reported in [46]. Loading of a single Yb^+ ion is completed by blocking the ionization beams after the single-step increase.

3.3 Fluorescence detection

We detect the fluorescence emitted for a spontaneous decay from the $^2P_{1/2}$ to the $^2S_{1/2}$ states upon driving the $^2S_{1/2} - ^2P_{1/2}$ cooling transition, using a photomultiplier tube (PMT). The fluorescence detection systems in the two

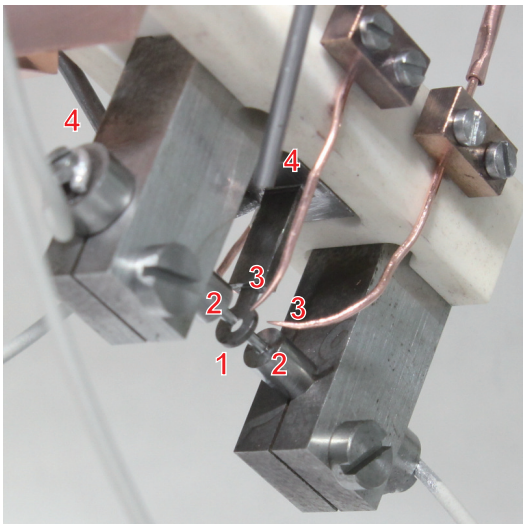

Figure 3.4: Picture of the RF trap used in this study (trap2). The numbers shows as follows: 1: ring electrode, 2: endcap electrodes, 3: compensation electrodes, 4: ytterbium oven. Two identical trap electrodes are used in this study, except that the edges of two compensation electrodes are wound in trap1.

trap apparatus are similar. The fluorescence generated by driving the cooling transition is corrected in a solid angle of 0.20 Sr, is focused on a pinhole of a diameter of 400 μm, and is detected by a photomultiplier using photon counting method. The output pulses from the PMT are amplified, discriminated from the dark noise, and shaped. The shaped pulses are counted by a universal counter (Agilent 53230a or Pendulum CNT-91). The overall fluorescence detection efficiency is 2.6×10^{-3}. We measure a typical count rate of 15000 per second when we laser-cool a single $^{174}Yb^{+}$ ion, after excess micromotions are minimized using a single cooling beam. For a single $^{171}Yb^{+}$ ion, the count rate decreases to 4000 per second because of the branches to the magnetic sublevels in the ground state [47].

3.4 System for spectroscopy

Schematic of the experimental setups for single-ion spectroscopy of the $^2S_{1/2} - {}^2D_{5/2}$ transition in $^{174}Yb^{+}$ and $^2S_{1/2} - {}^2D_{3/2}$ transition in $^{171}Yb^{+}$ are shown in Figs. 3.5 and 3.6, respectively.

For the $^2S_{1/2} - {}^2D_{5/2}$ transition in $^{174}Yb^{+}$, we mainly use trap2. All beams are transferred by polarization maintaining fibers. The cooling beam is divided into two beams. The first cooling beam is colinearly overlapped with a repumping beams by a dichronic mirror. The second cooling beam is propagated nearly perpendicular to the first cooling beam. The second cooling beam propagating in a different azimuthal angle to the trap axis is required to cool the degenerated radial secular motion when the trap has a rotational symmetry [48, 49]. The clock beam is colinearly propagating with the first cooling beam. The clock deexcitation beam is irradiated against the first cooling beam. The powers measured at the windows of the vacuum chamber and the beam diameter estimated at the trap are 3 μW, 30 μm; 3 mW, 200 μm; 500 nW, 100 μm; 250 μW, 80 μm; 300 μW, 100 μm; and 5 μW, 100 μm, for the cooling, repumping, clock, clock-deexcitation, first ionization, second ionization beams, respectively. The cooing beam is splitted to two beams of 1.5 μW when two beams are used for cooling. The polarization of each beam is adjusted using a half-wave plate. The polarizations of the repumping and clock beams are vertical to the magnetic field of 300 μT, which is applied vertically to the propagation directions of the cooling and clock beams.

For the $^2S_{1/2} - {}^2D_{3/2}$ transition in $^{171}Yb^{+}$, we use trap1. The beams for cooling, repumping, and clock excitation are transferred by the polarization-

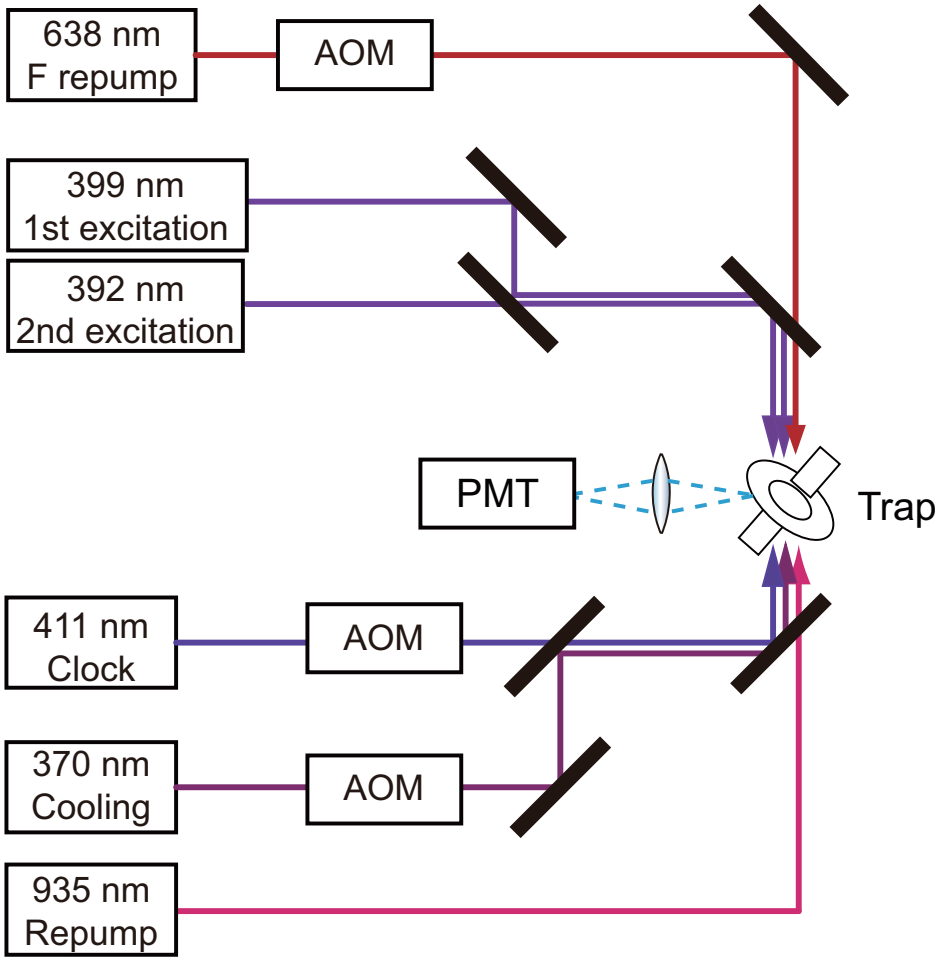

Figure 3.5: Schematic diagram of experimental setup for single-ion spectroscopy of $^2S_{1/2} - {}^2D_{5/2}$ transition in $^{174}Yb^+$.

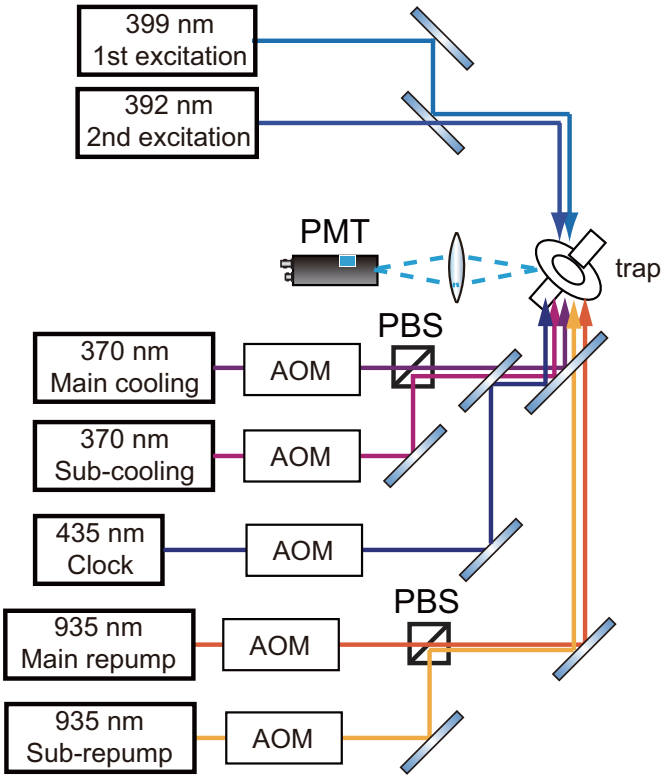

Figure 3.6: Schematic diagram of experimental setup for single-ion spectroscopy of $^2S_{1/2} - {}^2D_{3/2}$ transition in $^{171}\mathrm{Yb}^+$.

maintaining fibers, except for one single-mode fiber that is used for the sub-cooling beam, and collinearly overlapped by dichroic mirrors and polarization beam splitters. The beams for photoionization are combined in a polarization-maintaining fiber, and are introduced to the trap from the side opposite to the other beams. All beams are focused at the trap center. The beam diameters at the focal point (measured outside the trap apparatus) of the main and sub-cooling beams, the main and sub-repumping beams, and the clock beam are 60, 60, 190, 190, and 80 μm, respectively.

To conduct single-ion spectroscopy of the clock transitions in $^{174}Yb^{+}$ and $^{171}Yb^{+}$, the beams are sequentially introduced and blocked using AOMs, which are required for fast switching. Further, the dead time in interrogation sequence should be minimized to realize rapid detection of the spectra to realize a future plan of frequency stabilization. This is achieved using a digital delay generator configured by employing a field-programmable gate array (FPGA) board containing a processor (National Instruments myRIO) controlled by the LabVIEW program (National Instruments). The delay generator has eight outputs that can be simultaneously operated with a time resolution of 1 μs. The measurement sequence is initiated by sending a trigger to the board. The board then generates and transmits the pulse sequence to the AOMs according to the procedure described in each experimental chapter and sends a trigger pulse to the universal counter at the start of the state detection. The count result obtained with the programmable gate time is transferred to a computer via a GPIB cable. The state detection and calculation of the excitation probability are performed by the computer. The measurement with one clock-laser excitation is completed with a total dead time of approximately 4 ms. Then, the frequency of the clock laser is changed using the synthesizer via a LAN cable. The synthesizer is allowed a 10 ms settling time before the next measurement of the excitation probability is initiated. Note that the delays in communication through the GPIB and LAN cables(1 or 2 ms) are acceptable in this work.

Chapter 4

Laser cooling of single Yb ion

As described in Chapter 1, we investigate the condition of laser cooling using independent lasers for each related transitions as is different from previous work.

To obtain reference spectra free from the firest-order Doppler shift, we trap and laser cool single Yb^+ ions in Lamb-Dicke region. In Section 4.1, we describe how to load single Yb^+ ions, adjusting the magnetic field to maximize the fluorescence rate, and detection of RF-photon cross correlation used for minimization of excess micromotions. These are conducted using $^{174}Yb^+$, which has no hyperfine structures. In Section 4.2, we describe laser cooling of $^{171}Yb^+$, which has hyperfine structures but an useful isotope for optical clocks because it has magnetic-field insensitive clock transitions.

4.1 Laser cooling of $^{174}Yb^+$

4.1.1 Loading of single $^{174}Yb^+$ ions

$^{174}Yb^+$ ions are loaded through photoionization of ^{174}Yb atoms inside the trap. We generated a flux of Yb atoms by applying a current of 2.0 A to the Yb oven and conduct two-step photoionization [44]. We simultaneously irradiate with cooling and repumping beams. We can observe the fluorescence of the ionized Yb atoms. As the flux of Yb atoms is decreased, Yb^+ ions are sufficiently cooled and bright fluorescence was observed from Yb^+ ions concentrated to the center of the trap as a result of laser cooling. When we further decrease the flux of Yb atoms, we can load Yb^+ ions one-by-one. Figure 4.1 shows a sample of increase of the fluorescence with one-by-one loading.

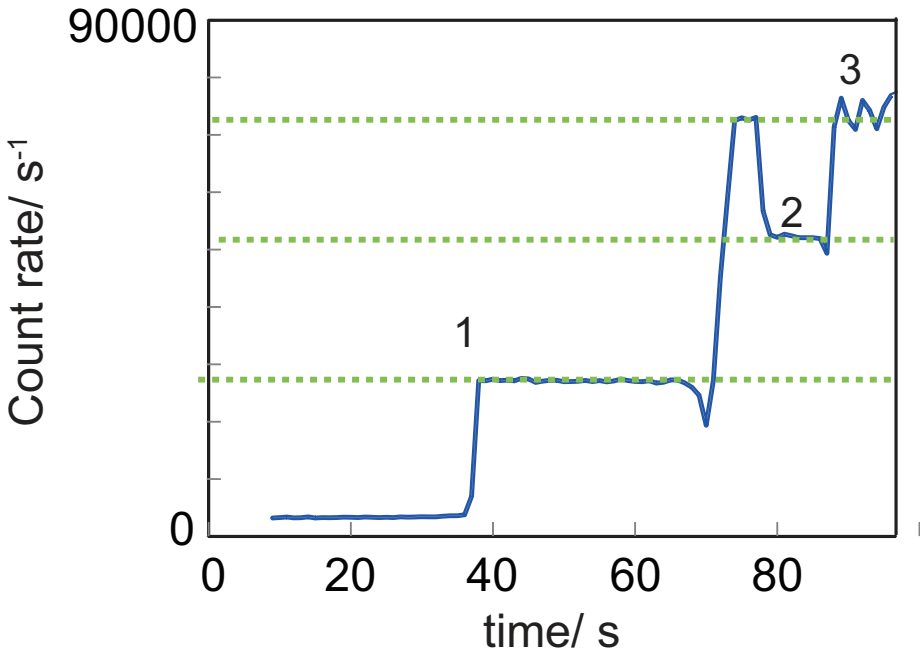

Figure 4.1: Increase of fluorescence caused by one by one loading of $^{174}Yb^{+}$ ions.

4.1.2 Adjustment of magnetic field

To apply a magnetic field of desired direction and strength, the ambient magnetic field at the position of the trapped ions is once canceled by observing the dark states in the ${}^2D_{3/2} - {}^3D[3/2]_{1/2}$ transition [50] as follows. First, we trap a single $^{174}Yb^{+}$ ion and observe the fluorescence. Then, we adjust the intensity of the magnetic field B_x along propagation of the repumping beam as the fluorescence intensity is minimized. Now, the direction of the residual ambient magnetic field is perpendicular to the repumping beam. Subsequently, we adjust the intensity of the magnetic field B_z perpendicular to the direction of polarization of the repumping beam. When the ambient magnetic field perpendicular to the polarization is removed, the fluorescence is minimized by optical pumping in the magnetic sublevels in the ${}^2D_{3/2}$ state. Finally, we rotate the polarization to 90° and adjust the magnetic field of residual direction B_y to minimize the intensity of fluorescence. The fluorescence intensity in near zero magnetic field is shown in Fig. 4.2.

4.1.3 Micromotion minimization using RF-photon correlation detection

As described in Section 2.1.1, excess micromotion minimization is almost always required for cooling of the ions confined in a RF trap. To reduce excess micromotions, we detect it using RF-photon correlation. In RF-photon correlation, we detect the change of the excitation probability caused by the change of the Doppler shift generated from the micromotion. The micromotion is forced motion by the AC driving field and is synchronized with the the AC driving voltage. We detect the correlation as follows. We start the time interval measurement when the photon of the fluorescence from the trapped ion is detected, and end it at the fixed phase, i.e., the upward zero crossing in our measurement, of the AC driving voltage of the trap. We repeat this time interval measurement and collect the number of trials that the measured time interval agrees with each time bin. We set the time bin to be 7.0×10^{-10} s corresponding to $\sim 1/100$ period of the AC driving voltage. We repeat the time interval measurement 20000 times to obtain the correlation. One correlation measurement consumes 10 s.

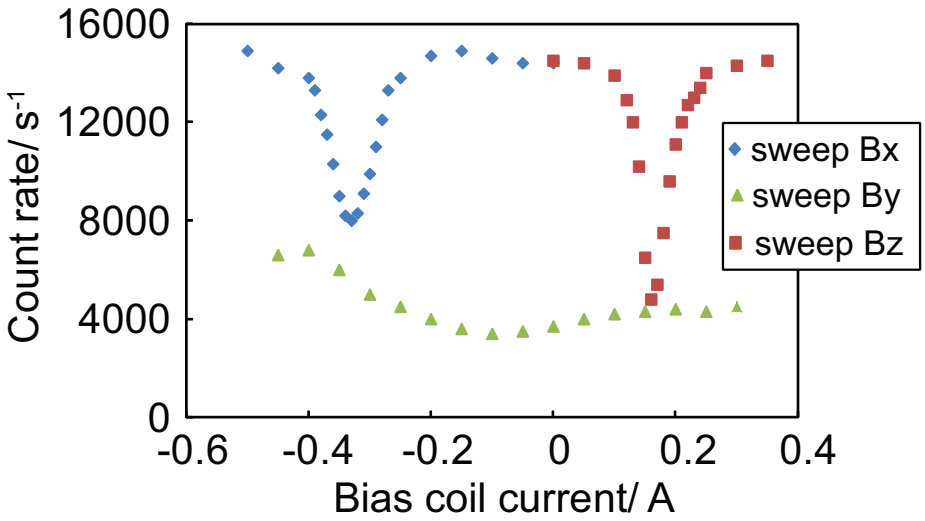

Figure 4.2: Fluorescence of $^{174}Yb^{+}$ near zero magnetic field, when intensity of applied magnetic filed was varied. The stray fluorescence level is approximately 3000. B_x: magnetic field along the propagation of repumping beam; B_y: magnetic field directed orthogonally to repumping beam in the horizontal plane; B_z: magnetic field directed along to vertical plane. First, we varied the intensity of B_x. Subsequently, we varied the intensity of B_z. Finally, we vareid the intensity of B_y after we adjusted the intensities of B_x and B_z to minimize the fluorescence intensity and rotated the polarization of the repumping beam to direct vertically to the direction of B_y.

4.2 Laser cooling of $^{171}Yb^{+}$

For efficient cooling of a $^{171}Yb^{+}$ ion by depletion of the $^{2}S_{1/2}$ state, we adjusted the power of the subcooling beam and simultaneously observed the fluorescence rate. The result is shown in Fig. 4.3. Only a few nanowatts were required for depletion of the $^{2}S_{1/2}(F = 0)$ state. We set the power of the subcooling beam to approximately 100 nW, which alleviated the frequency stability and tuning requirements, while still being sufficiently small to prevent the increase of any stray light.

4.2.1 Adjustment of magnetic field

We optimized the applied magnetic field to avoid optical pumping in the magnetic sublevels in the $^{2}S_{1/2}(F = 1)$ state. Note that optical pumping also occurs in the main repumping transition. To simplify the observation, we adjusted the polarization of the main repumping beam to that of the main cooling beam in every case. Further, it was necessary to remove the ambient magnetic field before application of an appropriate magnetic field. This was achieved as follows. The main cooling beam propagated parallel to the optical table on which the trap apparatus was placed. Thus, we defined the horizontal plane as that parallel to the table, for convenience of explanation.

First, we removed the component of the ambient magnetic field perpendicular to the beam propagation direction in the horizontal plane. We adjusted the magnetic field in the perpendicular direction as the fluorescence rate was minimized, while the polarization of the main cooling beam was set to horizontal. As a result, the direction of the residual ambient magnetic field was directed along the vertical plane, in accordance with the beam propagation direction. Then, we removed the component parallel to the beam propagation direction to extinguish the fluorescence, as described above, with the vertical polarization of the beam. The residual ambient magnetic field was then directed vertically. Then, we rotated the polarization to 45° and the fluorescence was recovered. Finally, we removed the vertical component to extinguish the fluorescence; the ambient magnetic field was completely removed.

Following cancellation of the ambient magnetic field, we applied a magnetic field vertically and observed the fluorescence rate as the polarization angle of the main cooling beam was rotated. At this stage, the main cooling beam power was at 3 μW at the trap chamber window. The results are

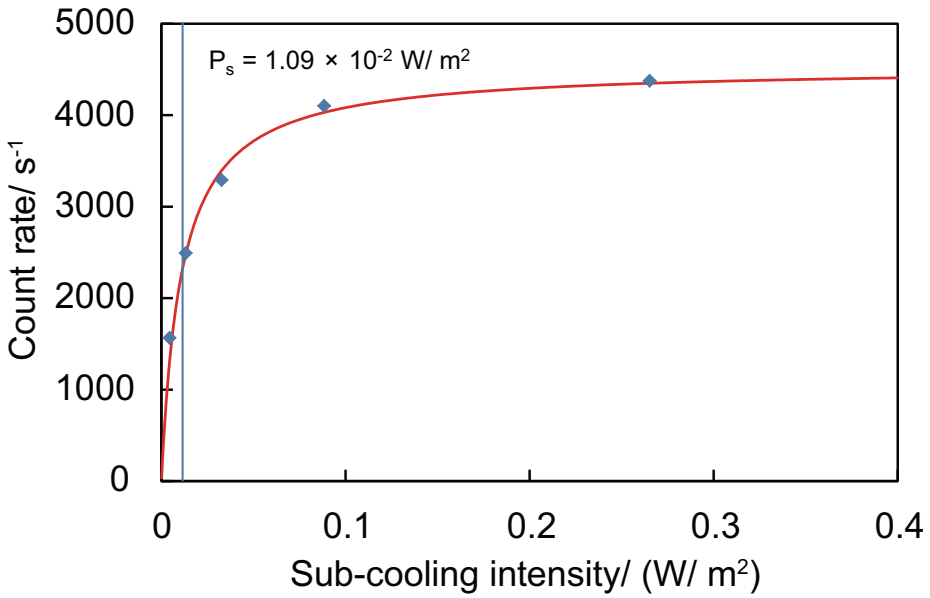

Figure 4.3: Dependence of fluorescence rate emitted from $^2P_{1/2}$ to $^2S_{1/2}$ state on sub-cooling beam power. The curved line shows the fitted function. The sub-cooling beam diameter is 60 μm. The saturation intensity is $1.09 \times 10^{-2}\,\mathrm{W/m^2}$.

shown in Fig. 4.4, in which the fitting curve was derived with reference to [50]. Note that the optimum magnetic field strength depends on the intensity of the main cooling beam [50]. We typically applied a magnetic field with a strength of more than $300\,\mu$T. Further, maximum suppression of the optical pumping theoretically occurs when the polarization angle of the main cooling beam is 55° relative to the magnetic field. Here, the magnetic field was applied at 45°, meaning that the fluorescence rate decreased by only 10 %.

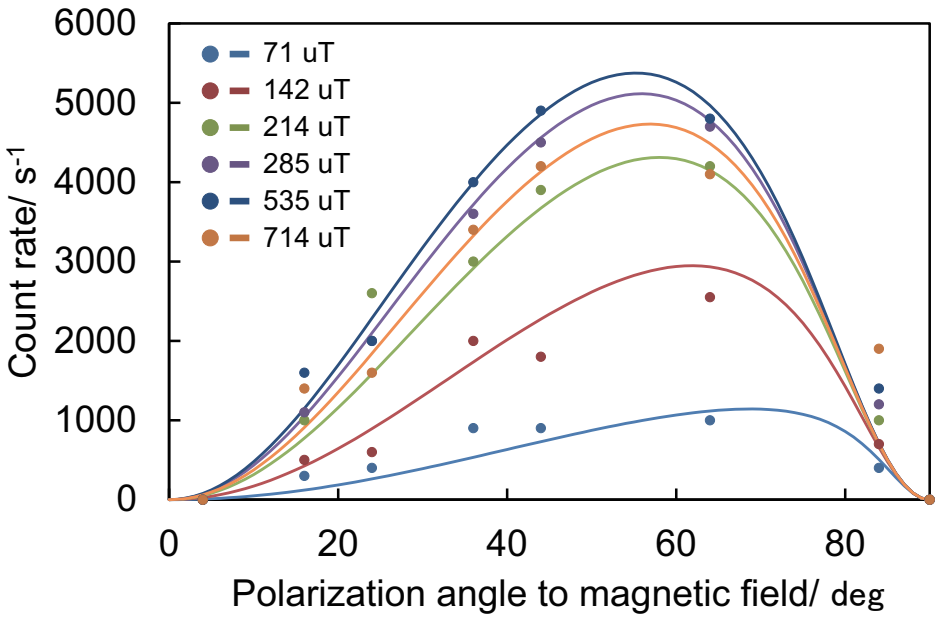

Figure 4.4: Dependence of cooling fluorescence on polarization angle of main cooling laser relative to magnetic field direction. The curved lines show the fitted functions, with reference to [50].

Chapter 5

Single-ion spectroscopy of $^2S_{1/2} - {}^2D_{5/2}$ clock transition in $^{174}\mathrm{Yb}^+$

We start single-ion spectroscopy from the $^2S_{1/2} - {}^2D_{5/2}$ transition in $^{174}\mathrm{Yb}^+$ to establish a spectroscopy system, because $^{174}\mathrm{Yb}^+$ has no hyperfine structure and the it is easy to detect the excitation to the $^2D_{5/2}$ state by observing electron shelving to the subsequent decay to the $^2F_{7/2}$ state of a very long lifetime. We select the Zeeman components of $\Delta m_j = \pm 2$ and further improve the resolution to detect the resolved motional sideband spectra of the $m_j = -1/2 - m_{j'} = -5/2$ transition from four components of $\Delta m_j = \pm 2$ transition as described in Section 5.2.

5.1 Interrogation sequence of the $^2S_{1/2} - {}^2D_{5/2}$ transition

Spectroscopy of the $^2S_{1/2} - {}^2D_{5/2}$ transition is conducted according to the sequence shown in Fig. 5.1. (1) A single $^{174}\mathrm{Yb}^+$ ion is laser cooled by irradiation with radiation at 370 nm and 935 nm. (2) The cooling beam at 370 nm is blocked to avoid light shift, and a clock pulse of radiation at 411 nm is applied during 5 ms. (3) Irradiation with radiation at 370 nm and 935 nm is conducted and the fluorescence is measured during a gate time of 10 ms for the state detection. If no fluorescence is detected, the excitation to the $^2D_{5/2}$ state is detected because of subsequent decay to the $^2F_{7/2}$ state. Then, the ion is deexcited from $^2F_{7/2}$ state to the $^2S_{1/2}$ state by irradiation with

radiation at 638 nm . The time required for the deexcitation is $\sim$ 100 ms. (4) Repeating the procedures (1)-(3) enables us to determine the excitation probability to the $^2D_{5/2}$ state. In our spectroscopy system, a measurement cycle with one clock-laser excitation of (1)-(3) is completed in 40 ms when a $^{174}Yb^+$ ion is not excited in the $^2D_{5/2}$ state. We perform this trial 50 times at a fixed frequency of the clock laser to determine the excitation probability. (5) Then, we measure the excitation probability as we frequency sweep the clock laser to obtain a spectrum in a single $^{174}Yb^+$.

5.2 Zeeman components and resolved-sideband spectra of $^2S_{1/2} - {}^2D_{5/2}$ transition

We conducted single-ion spectroscopy of the $^2S_{1/2} - {}^2D_{5/2}$ clock transition in $^{174}Yb^+$. The $^2S_{1/2} - {}^2D_{5/2}$ transition is composed of ten Zeeman components corresponding to $\Delta m_j = 0, \pm 1, \pm 2$ as shown in Fig. 5.2. First, to simplify observed spectra, we applied a small magnetic field perpendicular to the polarization of the clock laser to select the $\Delta m_j = \pm 2$ Zeeman components which include four transitions: $m_j = 1/2 - m_{j'} = -3/2$, $m_j = -1/2 - m_{j'} = -5/2$, $m_j = 1/2 - m_{j'} = 5/2$, and $m_j = -1/2 - m_{j'} = 3/2$ transitions as shown in Fig. 5.2. We probed the four components by applying the magnetic field of 70 μT with the clock-laser power of 30 μW. The result is shown in Fig. 5.3. When the magnetic field of 70 μT is applied, the splits of the components are calculated to be ± 2.0 MHz and ± 2.8 MHz with relative strength of 5/6 and 1/6, for $m_j = -1/2 - m_{j'} = -5/2$ and $m_j = 1/2 - m_{j'} = -3/2$ transitions, respectively. We observed an overlap of $\Delta m_j = \pm 2$ components caused by saturation broadening of the clock transition. Second, we changed the strength of applied magnetic field to 200 μT, and probed the same Zeeman components. We observed the partially resolved $\Delta m_j = \pm 2$ components as shown in Fig. 5.4. In this strength of magnetic field, the estimated splits are ± 5.6 MHz and ± 7.8 MHz, respectively.

Finally, we reduced the clock-laser power to 1 μW and probed the $m_j = -1/2 - m_{j'} = -5/2$ transition in $\Delta m_j = -2$ components with a resolution of 2 kHz. The result is shown in Fig. 5.5. Motional sidebands were resolved from the carrier by the intervals of secular frequencies of several hundreds hertz. The spectral width of the carrier spectrum was 20 kHz.

The asymmetry in the Zeeman components and the resolved-sideband spectra shown in Fig. 5.3 $\sim$ 5.5 were caused by the drift of the master laser in the clock laser system. The compensation of this drift is introduced in the

subsequent Chapters and the details are described in Section 6.3.2.

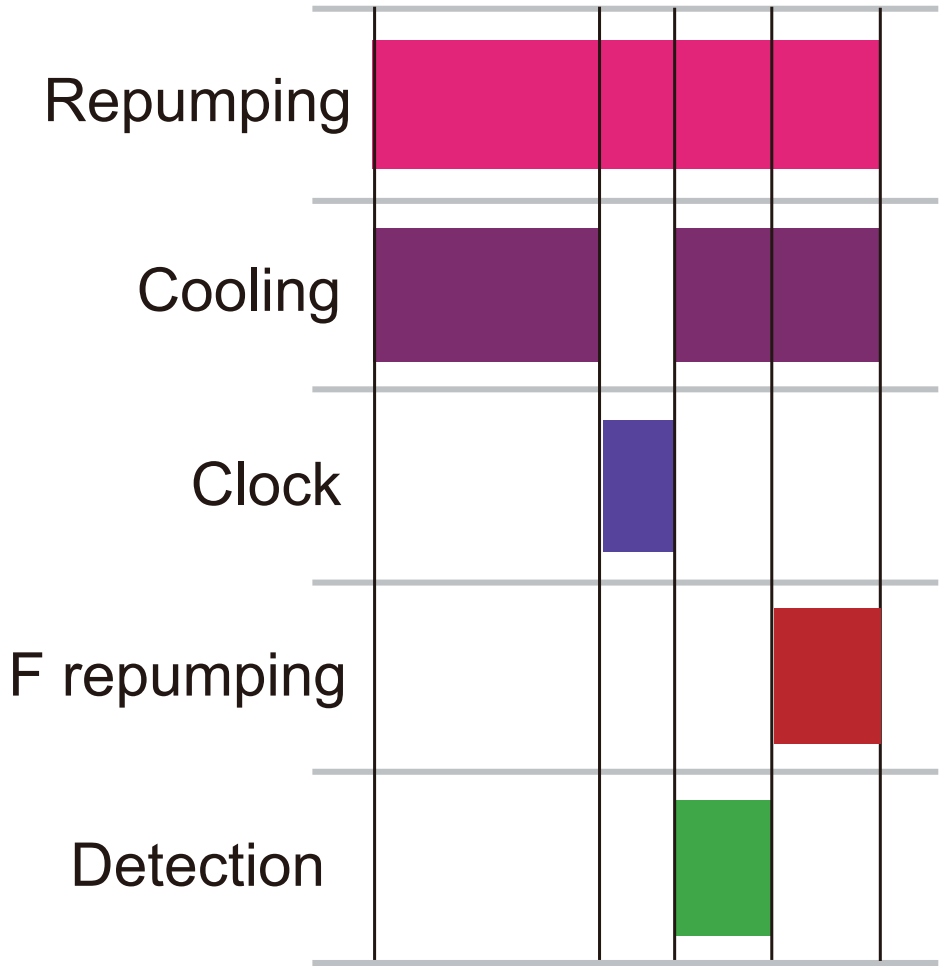

Figure 5.1: Interrogation sequence for spectroscopy of $^2S_{1/2} - ^2D_{5/2}$ transition.

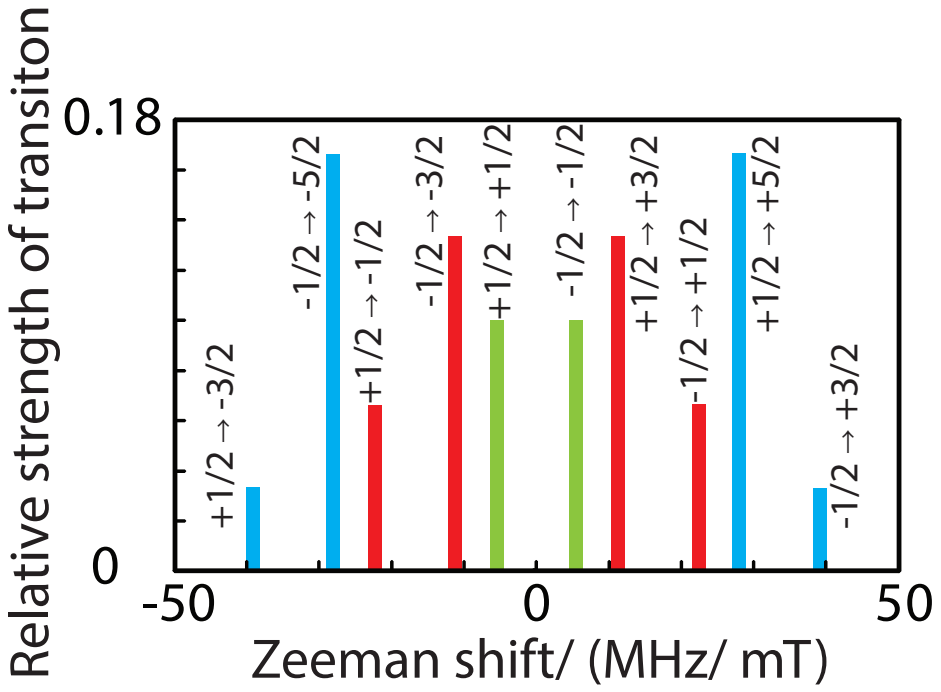

Figure 5.2: All Zeeman components of ${}^2S_{1/2} - {}^2D_{5/2}$ transitions. The green components represent $\Delta m_j = 0$, the red components represent $\Delta m_j = \pm 1$, and the blue components represent $\Delta m_j = \pm 2$ transitions.

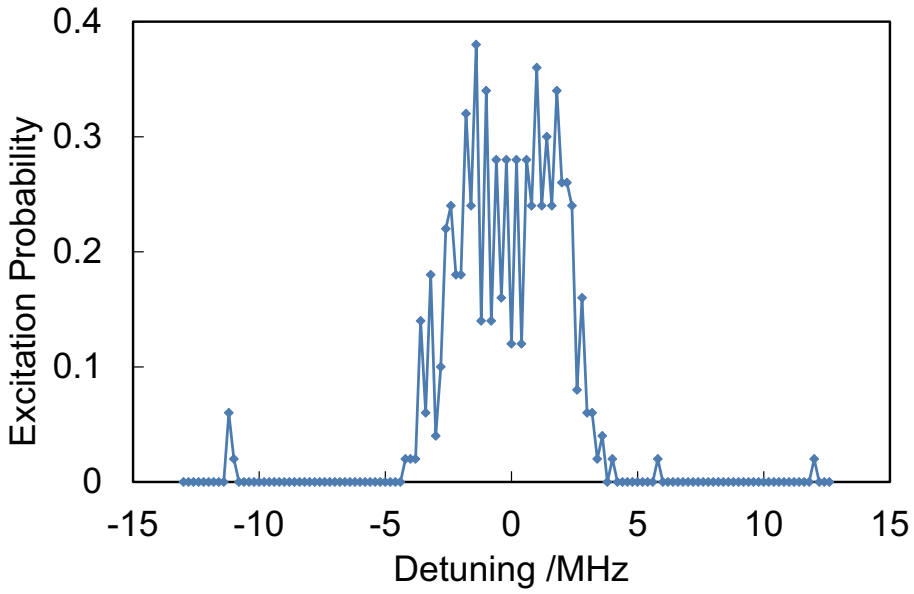

Figure 5.3: $\Delta m_j = \pm 2$ Zeeman components of the $^2S_{1/2} - {}^2D_{5/2}$ transition in a magnetic field of 70 μT. The frequency interval is 200 kHz. The excitation probability is determined from 50 clock-laser excitation.

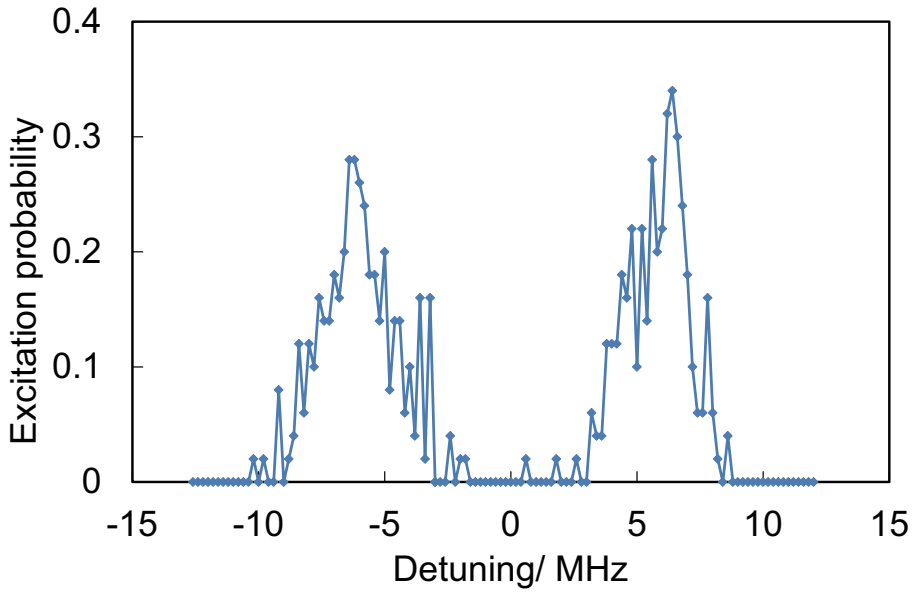

Figure 5.4: $\Delta m_j = \pm 2$ Zeeman components of the $^2S_{1/2} - {}^2D_{5/2}$ transition in a magnetic field of 200 μT. The frequency interval is 200 kHz. The excitation probability is determined from 50 clock-laser excitation.

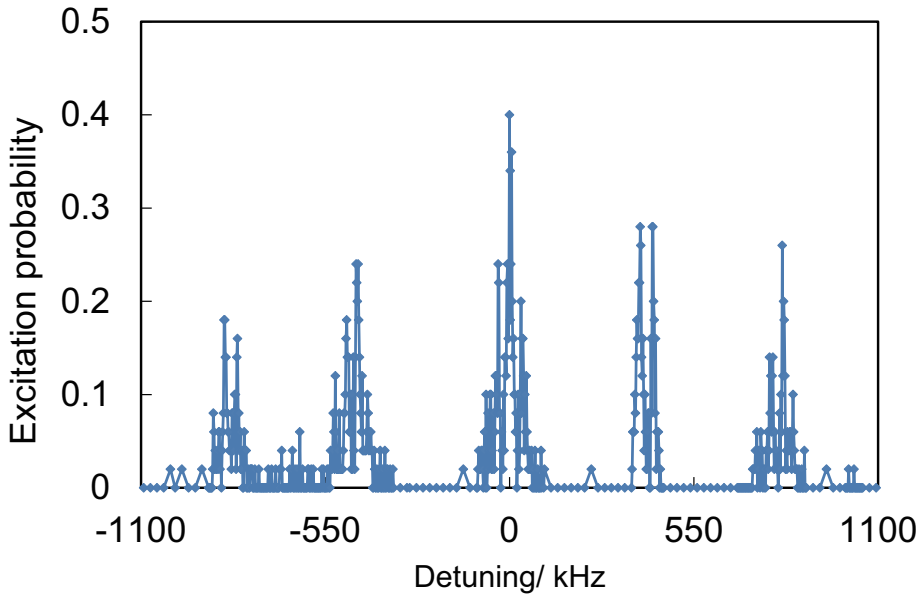

Figure 5.5: Carrier and resolved-sideband spectrum of $m_j = -1/2 - m_{j'} = -5/2$ transition in $\Delta m_j = -2$ components. The frequency interval is 2 kHz. The excitation probability is determined from 50 clock-laser excitation.

Chapter 6

Single-ion spectroscopy of $^2S_{1/2}-{}^2D_{3/2}$ clock transition in $^{171}\mathrm{Yb}^+$

In this chapter we describe our scheme and results of single-ion spectroscopy of the $^2S_{1/2}(F=0)-{}^2D_{3/2}(F'=2)$ clock transition in $^{171}\mathrm{Yb}^+$. Spectroscopy of the clock transition requires decoupling of the $^2D_{3/2}(F=2)$ state from the laser-cooling cycle. We investigate this decoupling of the $^2D_{3/2}(F=2)$ state by using independent light sources for driving of all the transitions between the hyperfine structures contained in the cooling and repumping transitions. We increase the resolution of the spectroscopy to the Zeeman components and the motional sideband of the $m_F=0-m_{F'}=0$ magnetic-insensitive transition. We investigate the carrier spectra of this clock transition with the best resolution at this moment by removing the frequency drift of the clock laser.

6.1 Preparation for spectroscopy: decoupling $^2D_{3/2}(F=2)$ state from cooling cycle

To conduct single-ion spectroscopy of the $^2S_{1/2}(F=0)-{}^2D_{3/2}(F'=2)$ transition, we must decouple the $^2D_{3/2}(F=2)$ state from the cooling cycle [17]. For this purpose, we blocked the subrepumping beam and adjusted the power of the main repumping beam. When the power of the latter was sufficiently large, saturation broadening and off-resonant excitation depleted the $^2D_{3/2}(F=2)$ state, as shown in Fig. 6.1(a). Dark periods were observed

in the fluorescence as the power of the main repumping beam was decreased, which were caused by population of the $^2D_{3/2}(F = 2)$ state, as shown in Fig. 6.1(b). Detection of the dark period enabled us to detect the ions in the $^2D_{3/2}(F = 2)$ state. As regards the fluorescence rate, a minimum gate time of 10 ms was required to determine the dark duration. We measured the rate of detection of the dark periods as a function of the power of the main repumping beam to investigate the appropriate power range of that beam. The result is shown in Fig. 6.2. As the power of the main repumping beam was decreased to below 50 μW, the fluorescence rate decreased as a result of the slow repumping rate. Therefore, we adjusted the power of the main repumping beam to 200 μW.

6.2 Procedure of spectroscopy of $^2S_{1/2} - ^2D_{3/2}$ transition

The interrogation sequence shown in Fig. 6.3 is as follows: (1) a single $^{171}Yb^+$ ion is irradiated with the main and subcooling lasers, and with the main repumping laser for 20 ms to cool the ion; (2) the subcooling laser is blocked for 10 ms in order to initialize the $^{171}Yb^+$ ion to the $^2S_{1/2}(F = 0)$ state. The initialization time of 10 ms was determined as described later; (3) the main cooling laser and the main repumping laser are intercepted and the probe laser pulse is applied; and (4) the main and subcooling lasers, and the main repumping laser are introduced for state detection. The state detection is performed using the fluorescence rate observed for a 10 ms gate time. No fluorescence is observed when the $^{171}Yb^+$ ion is excited to the the $^2D_{3/2}$(F=2) state. We observe the fluorescence rate repeatedly with the 10 ms gate time until the fluorescence recovers. Then, we repeat the cycles from (1) to (4) and determine the transition probability. In our spectroscopy system, a measurement cycle with one clock-laser excitation is completed in 50 ms when a $^{171}Yb^+$ ion is not excited in the $^2D_{3/2}(F = 2)$ state. Several-tens of measurements are repeated to determine the excitation probability. Next, we obtain the spectrum via measurement of the transition probability during sweeping of the probe laser frequency. As the subrepumping beam is not required for cooling of the $^{171}Yb^+$ ion, we block the subrepumping beam during the spectroscopy after loading. Note that the subrepumping beam is useful for accelerating the detection cycle by clearing the $^2D_{3/2}(F = 2)$ state after the state detection. Further, in our present measurement scheme, we must wait for the period in which the $^{171}Yb^+$ ion remains in the $^2D_{3/2}(F = 2)$

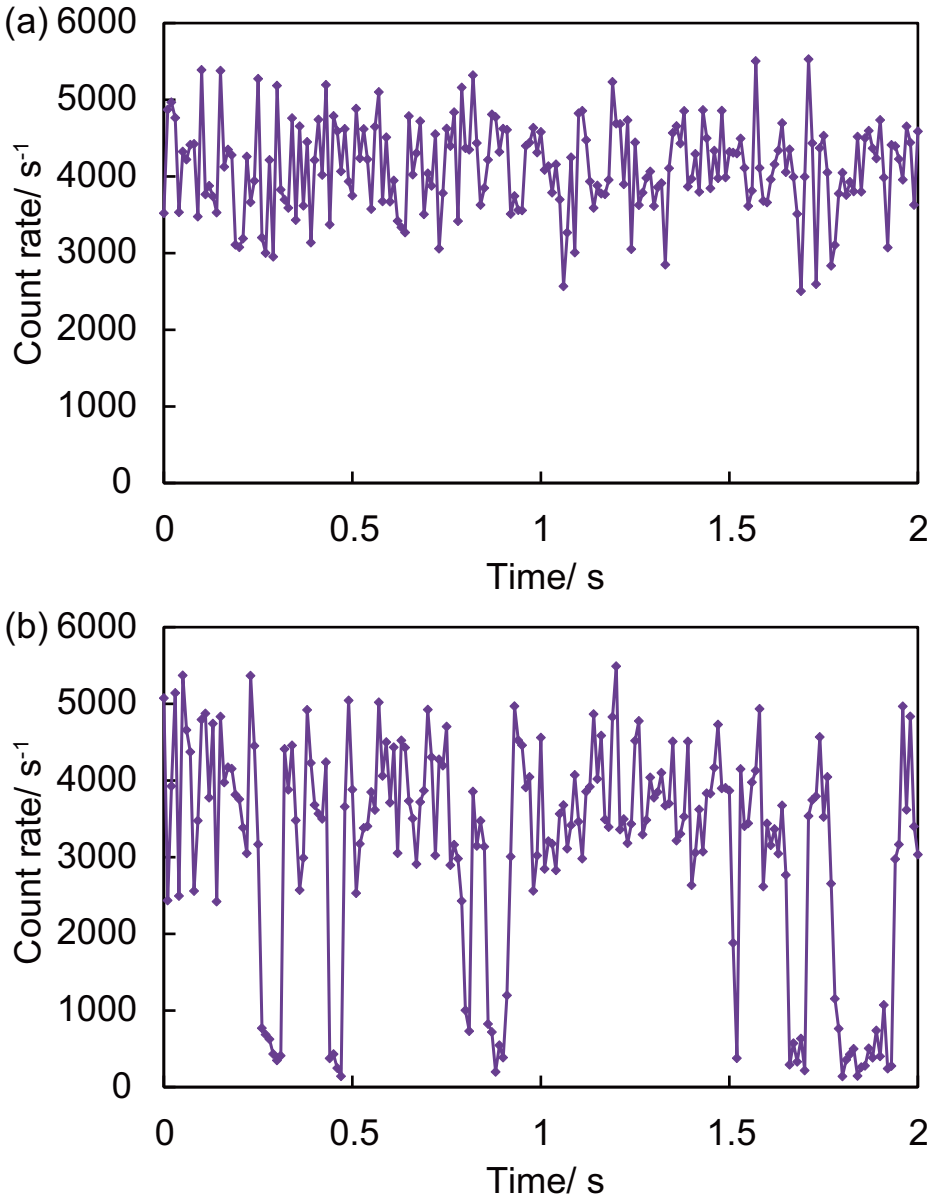

Figure 6.1: Fluorescence rate with 10-ms gate time for main repumping beam powers of (a) 9.5 mW and (b) 270 μW. For a sufficiently large power, the $^2D_{3/2}(F = 2)$ state is depleted by saturation broadening and off-resonant excitation, as shown in (a). By adjusting the power, pumping to the $^2D_{3/2}(F = 2)$ state via spontaneous decay from the $^2P_{1/2}(F = 1)$ state is detectable as dark periods.

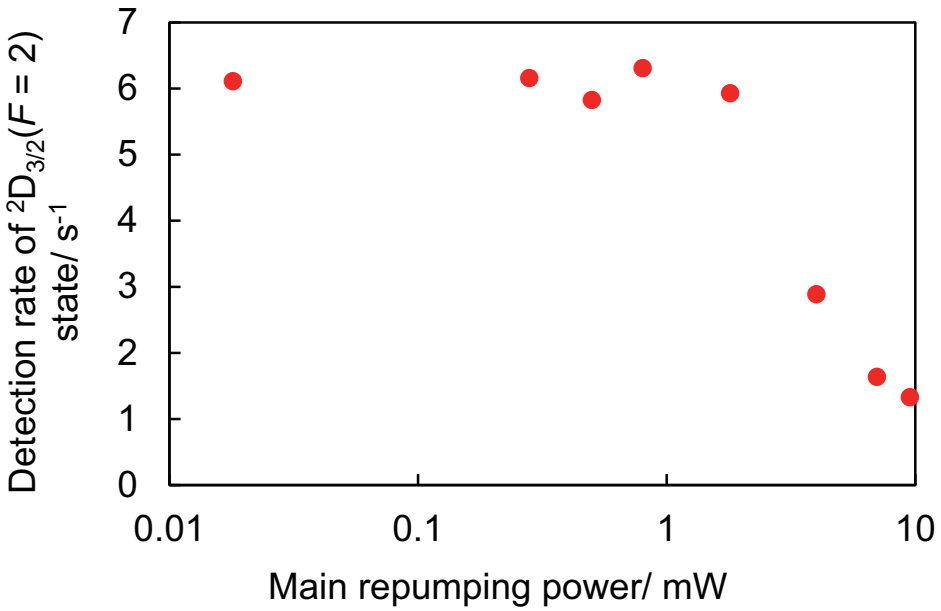

Figure 6.2: Relation between main repumping beam power and rate of spontaneous decay to $^2D_{3/2}(F = 2)$ state.

state for a lifetime of 52 ms [36].

For the procedure (ii), we determined the blocking duration of the subcooling beam required for initializing a single $^{171}Yb^+$ ion in the $^2S_{1/2}(F=0)$ state. We measured the decrease of the fluorescence rate after the subcooling beam was blocked. The result is shown in Fig. 6.4. This is similar to that reported in [46]. We fixed the blocking duration of the subcooling beam to be 10 ms in order to complete the initialization.

6.3 Spectra of $^2S_{1/2}(F=0)-{}^2D_{3/2}(F'=2)$ transition

6.3.1 Zeeman components and resolved-sideband

The $^2S_{1/2}(F=0)-{}^2D_{3/2}(F'=2)$ transition is composed of five Zeeman components corresponding to $\Delta m_F = 0, \pm 1, \pm 2$ transitions. In this study, in order to identify the $m_F = 0-m_{F'} = 0$ magnetic-insensitive component, we probed the entire Zeeman structure via frequency sweeping of the clock laser over a large span of approximately ± 20 MHz. We applied a magnetic field of 800 μT to resolve the Zeeman components, although the fluorescence rate was somewhat decreased. The magnetic field was directed at 45° from the vertical direction to the beam propagating direction. The polarization of the clock beam (and, also, the main cooling beam) was vertical. The results are shown in Fig. 6.5. The $m_F = 0 - m_{F'} = 0$ component was identified as the center component. Note that spontaneous decay from the $^2P_{1/2}(F=1)$ to the $^2D_{3/2}(F=2)$ state was detected, even during the state detection. This caused an offset of 0.08 in the excitation probability.

Then, we conducted spectroscopy of the $m_F = 0-m_{F'} = 0$ component and resolved sidebands generated from the axial and radial secular motions, as shown in Fig. 6.6. From the relative intensity of the sidebands to the carrier spectrum, we could estimate the temperature of a single $^{171}Yb^+$ ion. Although the frequency sweep involving 20 kHz intervals was too coarse for a precise estimation, we roughly determined the temperature to be approximately 7 mK.

6.3.2 Carrier spectrum of $m_F = 0-m_{F'} = 0$ component

Finally, we probed the carrier spectrum of the $m_F = 0-m_{F'} = 0$ component with higher resolution. Before performing a high-resolution scan, we mea-

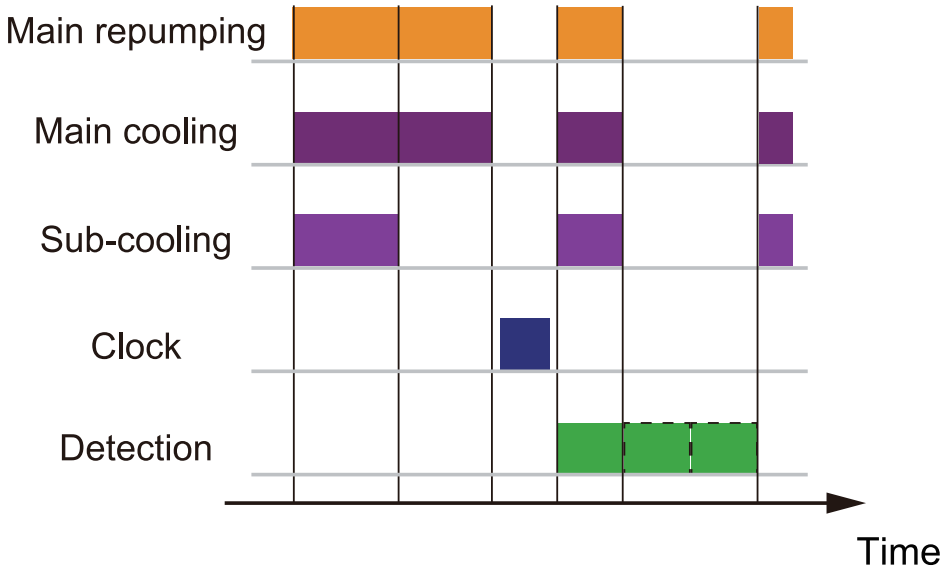

Figure 6.3: Time sequence for spectroscopy of $^2S_{1/2}(F=0)-^2D_{3/2}(F'=2)$ transition.

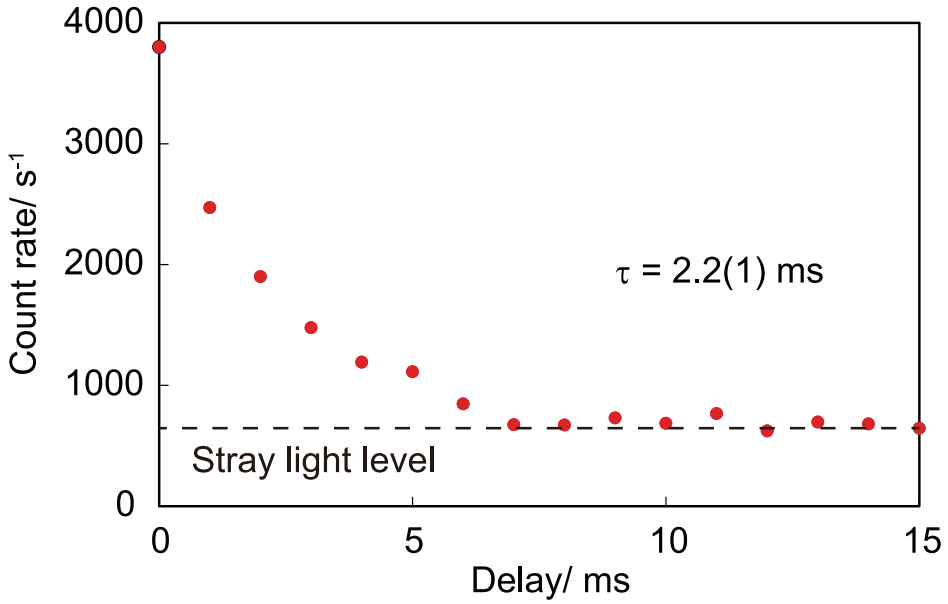

Figure 6.4: Measurement of pumping rate to $^2S_{1/2}(F = 0)$ state. Fluorescence decay caused by pumping to $^2S_{1/2}(F = 0)$ state after subcooling beam is blocked. The pumping time is determined to be 2.2(1) ms.

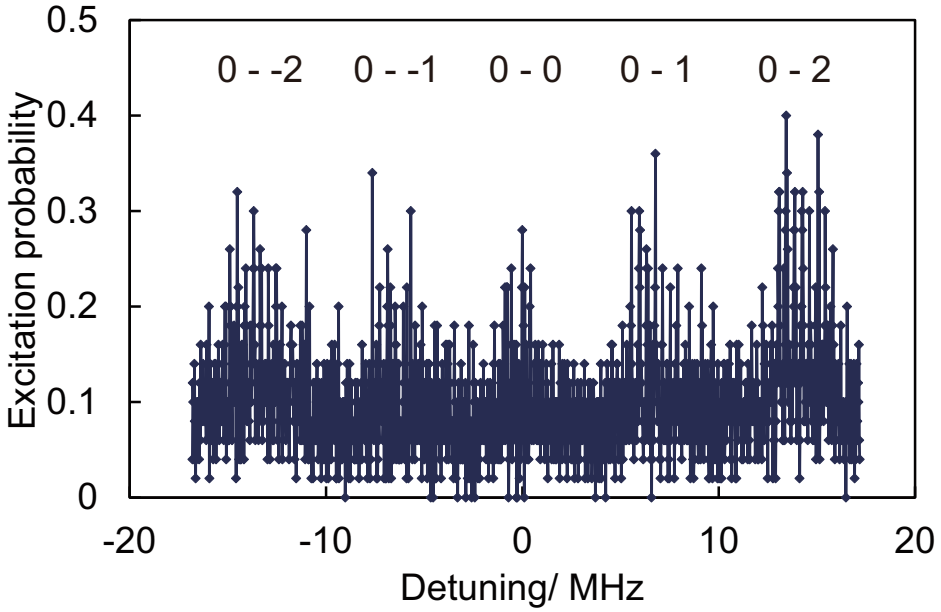

Figure 6.5: All Zeeman components of $^2S_{1/2}(F=0)-{}^2D_{3/2}(F'=2)$ transition are detected using a single $^{171}Yb^+$ ion. The frequency interval and excitation duration of the clock laser are 20 kHz and 10 ms, respectively. The excitation probability is determined from 50 measurements of the excitation at a single fixed probing frequency.

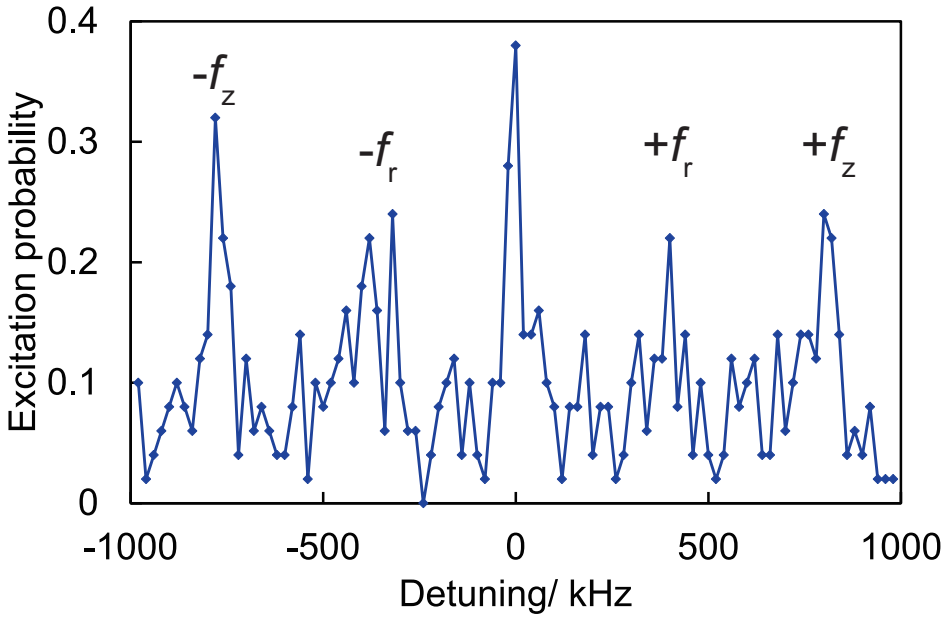

Figure 6.6: Resolved motional sidebands in $m_F = 0 - m_{F'} = 0$ component of $^2S_{1/2}(F=0) - ^2D_{3/2}(F'=2)$ transition. The frequency interval and excitation duration of the clock laser are 20 kHz and 10 ms, respectively. The excitation probability is determined from 50 measurements of the excitation at a single fixed probing frequency. The magnetic field is 600 μT.

sured the linear frequency drift of the clock laser by detecting the carrier spectra a small number of times at various intervals. The drift was feed-forward compensated by 32 Hz in 1 s intervals while the frequency sweeping of the clock laser was being conducted. Then, we recorded the carrier spectra twice by changing the frequency sweep direction of the clock laser to cancel any residual linear frequency drift as shown in Fig. 6.7. We obtained the spectrum shown in Fig. 6.8 after the drift cancellation. The full width at half maximum of this spectrum is 380 Hz.

We suppose that the possible contributions to the spectral width are the linewidth and stabilization of the clock laser, estimated to be 500 Hz (as shown in Ch. 3), the Fourier transform limit of 200 Hz, and the feed-forward compensation step of 32 Hz. Therefore, the observed spectral width is somewhat narrower than expectation. The clock-laser linewidth was estimated from half the beatnote between two systems. We assume that the linewidth of the clock laser used for spectroscopy should be superior to that of the other system used for linewidth estimation. The natural linewidth of the ${}^2S_{1/2}-{}^2D_{3/2}$ transition is 3 Hz [36]. Therefore, we require hertz-level linewidth in the clock laser. This simultaneously allows us to extend the excitation duration and decrease the Fourier transform limit. We will improve the isolation from vibrational and acoustic noise on the cavity resonance as we refer to the clock lasers used in the optical clocks with uncertainties of 10^{-18}.

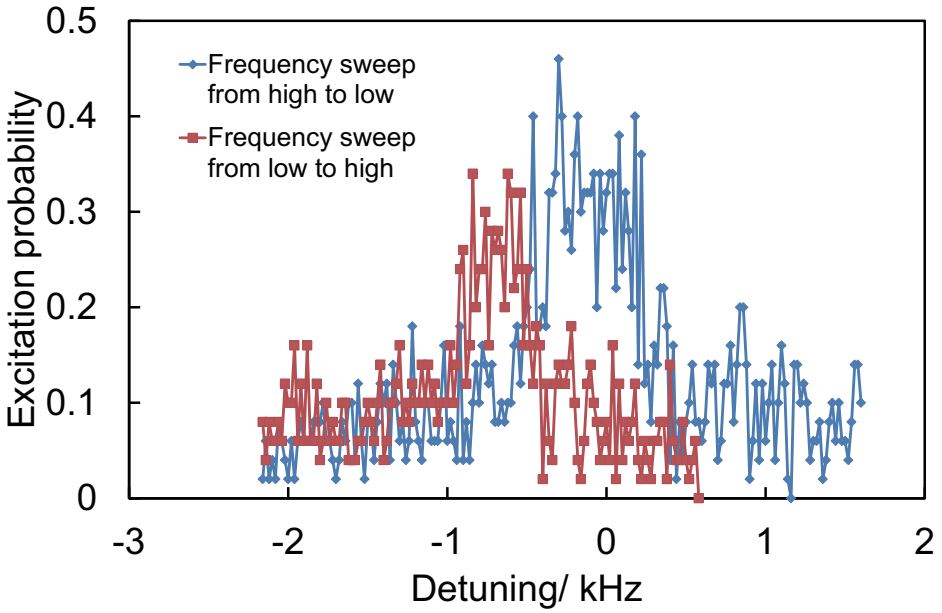

Figure 6.7: Carrier spectrum of $m_F = 0 - m_{F'} = 0$ component after cancellation of linear drift in clock laser. The frequency interval and excitation duration of the clock laser are 20 Hz and 5 ms, respectively. The excitation probability is determined from 50 measurements of the excitation. The clock frequency is feed-forward compensated by 32 Hz in 1 s intervals during measurement.

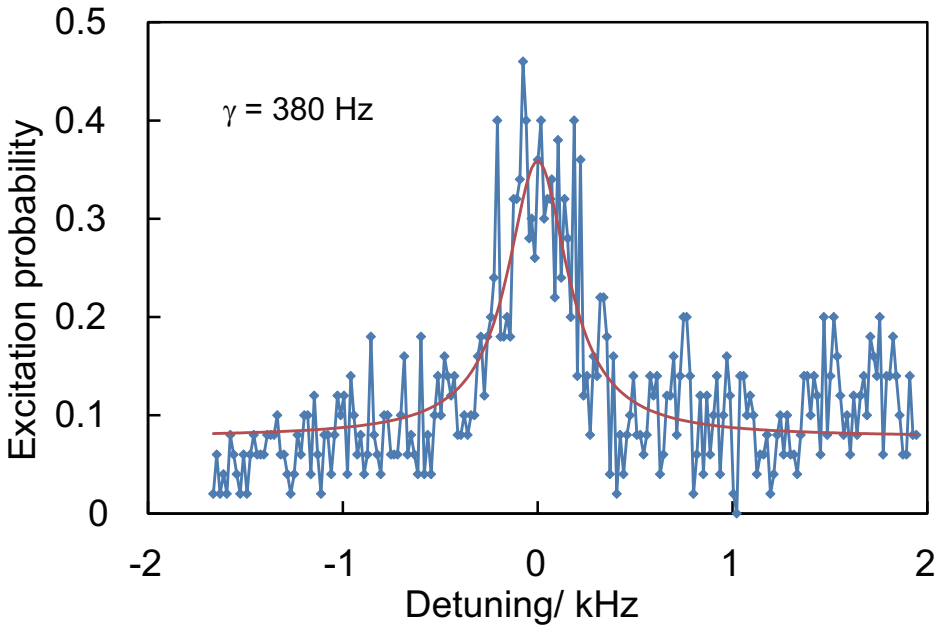

Figure 6.8: Carrier spectrum of $m_F = 0 - m_{F'} = 0$ component after cancellation of linear drift in clock laser. The frequency interval and excitation duration of the clock laser are 20 Hz and 5 ms, respectively. The excitation probability is determined from 50 measurements of the excitation. The clock frequency is feed-forward compensated by 32 Hz in 1 s intervals during measurement.

Chapter 7

Resolved-sideband spectra and minimization of excess micromotions

The translational energy of a trapped single-ion causes second-order Doppler shift, which is a major factor of the uncertainty of an optical clock. To evaluate the translational energy, the relative intensities of the sidebands in the resolved-sideband spectra is measured [51]. The precise measurement of the resolved-sideband spectra is also important for a π-pulse excitation using the carrier transition and for sideband cooling using the lower first sideband. In this chapter, we conduct precise measurements of the resolved-sideband spectra in single ions using the ${}^2S_{1/2} - {}^2D_{5/2}$ transition in ${}^{174}\mathrm{Yb}^+$ ions with higher resolution than that described in Chapter 5. This study was first motivated to reveal the origin of the subsidebands accompanied with the carrier spectra at a few tens kHz offset. From high resolution scanning of the entire resolved-sidebands, however, we found that all sidebands had structures of subsidebands.

In this chapter, we investigate the structures in the resolved-sideband spectra. We measured the dependence of frequencies of the sidebands on the trap parameters. We revealed that mixing of phase modulation by the secular motions in the different directions generated the subsideband structures. Therefore, we supposed that improvement of the micromotion minimization simultaneously reduce the structures in the resolved-sideband spectra. We described the detailed investigation of the relation between micromotion minimization and the structure. We found that not only the subsideband but also the secular motions were reduced after micromotions were minimized in

all-degree of freedom.

7.1 Resolved-sideband spectra with one-directional micromotion minimization

First, we introduced only the first cooling beam into the trap. We eliminated the RF-photon correlation by adjusting the compensation voltage applied to the one of the endcap electrodes. We conducted single-ion spectroscopy of the ${}^2S_{1/2}-{}^2D_{5/2}$ transition using the clock laser beam colinearly introduced with the cooling beam. We show a spectrum of the $m_j = -1/2$-$m_j = -5/2$ component in the ${}^2S_{1/2}-{}^2D_{5/2}$ transition in Fig. 7.1, and the RF-photon correlation signal in Fig. 7.2 when the spectrum was detected. The frequency drift of the clock laser was feedforward compensated during the frequency scanning as introduced in Chapter 6. We resolved motional sidebands in the spectrum caused by the axial and the radial secular motions. Moreover, we observed structures in the carrier and the sidebands in the spectrum.

To reveal the origin of the structures, we measured the RF resonance caused by the motions of a trapped ion. We applied a probe RF voltage between the endcap electrodes. The motions of the trapped ion are excited when the frequency of the probe RF voltage agrees with that of one of the ion motions. This results in the disappearance of the fluorescence. When the trap potential has anharmonicities, the radial and axial secular motions are coupled as shown in Eq. (2.11). This enables us to detect the radial secular motion and the nonlinear motions by increasing the amplitude of the probe RF voltage, even when the probe is applied in the axial direction [25].

To identify the motions detected by the RF resonance, and to investigate which sidebands in the spectra were identified with the RF resonances, we measured the dependence of the RF resonances and the resolved-sideband spectra on V_{AC}. The results are shown in Fig. 7.3. We could easily identify the axial secular frequency f_z because it was excited by a small probe RF voltage. We detected two more weaker RF resonances of the frequencies f_1 and f_2 (we defined as $f_1 < f_2$.) and identified the corresponding sidebands in the spectra, as indicated in Figs. 7.1 and 7.3.

The identification of the motions with f_1 and f_2 according to the dependence on V_{AC} was enabled by two factors: f_r and $f_z - f_r$, or f_x and f_y. The latter shows a breaking of the axial symmetry. To determine the appropriate factor, we measured the dependencies of the RF resonances on V_{DC}. In the former case, f_1 and f_2 show the opposite dependence on V_{DC}. In the latter,

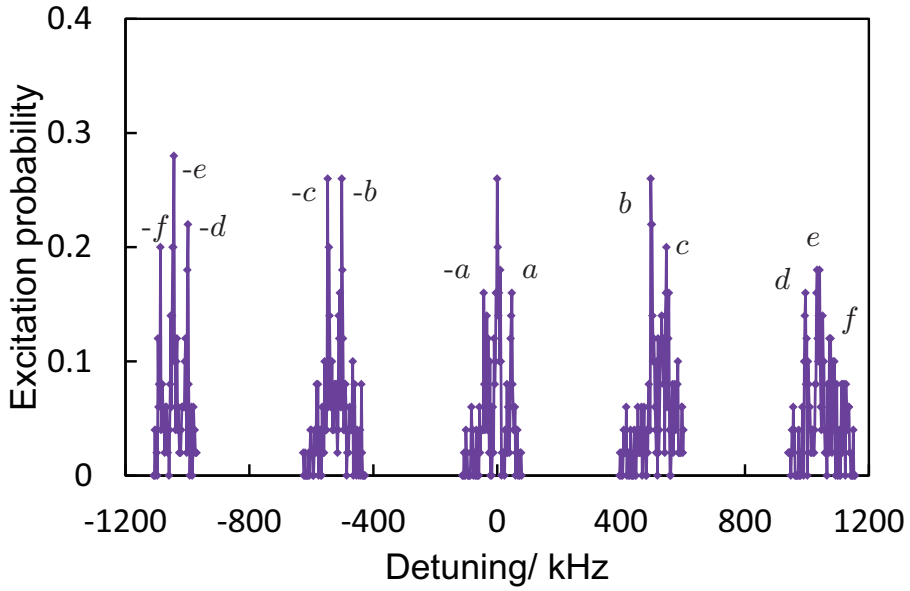

Figure 7.1: Resolved-sideband spectrum of ${}^2S_{1/2}(m_j = -1/2) - {}^2D_{5/2}(m_{j'} = -5/2)$ transition in single ${}^{174}\mathrm{Yb}^+$, when excess micromotions were minimized by eliminating RF-photon correlation detected using only one cooling beam. The secular and nonlinear-coupled frequencies generating the sidebands are identified in the figure: $a = f_z - 2f_r$, $b = f_r = f_1$, $c = f_z - f_r = f_2$, $d = 2f_r$, $e = f_z$, $f = 2(f_z - f_r)$. The identification method is described in the text.

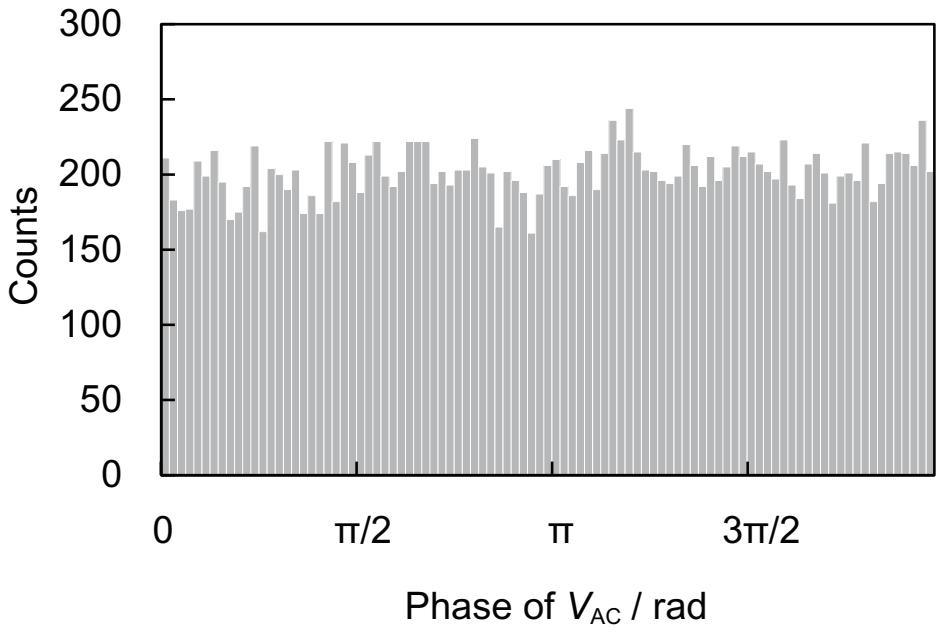

Figure 7.2: RF-photon correlation signal when the spectrum shown in 7.1 was detected. We show the correlation during close to one period of the AC driving voltage.

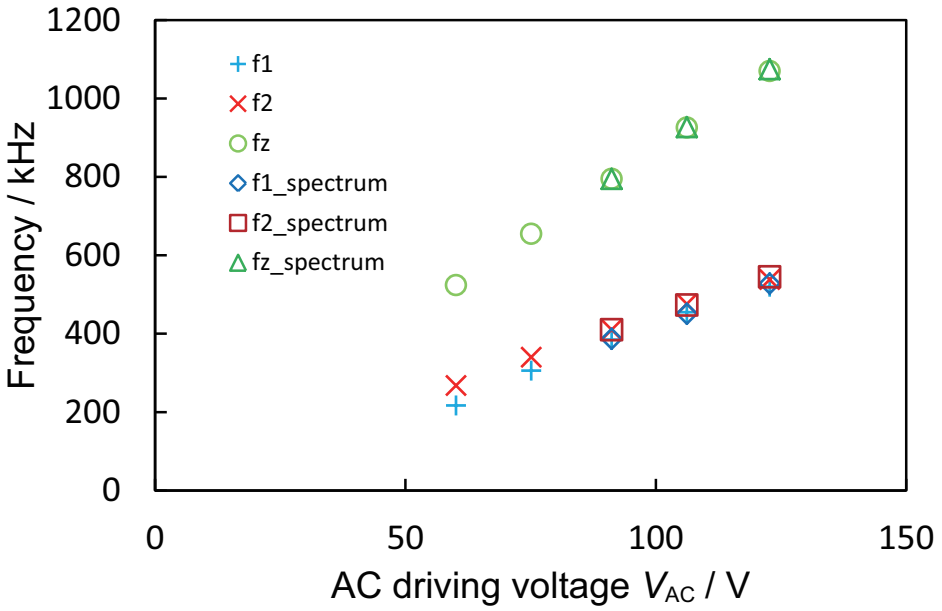

Figure 7.3: RF resonance frequency as a function of V_{AC}. Offset frequencies of the corresponding sidebands from the carrier observed in the resolved sideband spectra are shown as well. The probe RF voltage was applied between the endcap electrodes to detect the RF resonance. Two weak resonances were assigned as f_1 (plus marks) and f_2 (crosses) (we defined them as $f_1 < f_2$). The strong resonance was identified with the axial secular motion f_z (circles). The corresponding offset frequencies of the sidebands in the spectra are indicated with diamonds, rectangles, and triangles for f_1, f_2, and f_z, respectively.

the same dependence. As shown in Fig. 7.4, f_1 and f_2 show an opposite dependence and $f_1 + f_2 = f_z$. In addition, according to Eqs. (2.3) and (2.6), f_z and f_r shows the opposite dependence on V_{DC}. Therefore, we concluded that $f_1 = f_r$ and $f_2 = f_z - f_r$. Because we revealed that one of the large subsidebands was caused by a coupled motion of $f_z - f_r$, we assumed that the other subsidebands were also caused by mixing of the axial and radial secular motions. The identification of the motions is shown in Fig. 7.1. We confirmed the validity of this identification from the dependence of each sideband frequency on V_{AC}. The observed subsideband structures are generated from mixing of the phase modulations caused by the secular motions in different directions when the modulation index are large, *i.e.*, the single ion is confined out of the Lamb-Dicke region. The electric field in the laser of which frequency ω_{L} modulated by the radial and axial secular frequencies of ω_r, ω_z is described as

$$\begin{aligned} E_{\mathrm{L}} =& E\cos(\omega_{\mathrm{L}}t + m_1\cos\omega_r t + m_2\cos\omega_z t) \\ =& E\{\cos\omega_{\mathrm{L}}t\cos(m_1\cos\omega_r t + m_2\cos\omega_z t) \\ & - \sin\omega_{\mathrm{L}}t\sin(m_1\cos\omega_r t + m_2\cos\omega_z t)\}. \end{aligned} \tag{7.1}$$

The laser phase modulated by secular frequencies of ω_r, ωz generates the beats between the laser frequency of ω_{L} and the secular frequencies. For a small modulation indexes, *i.e.*, $m_1,\ m_2 \ll 1$, the Eq. 7.1 can be approximated using the first-order term as

$$\begin{aligned} E_{\mathrm{L}} \simeq E\cos\omega_{\mathrm{L}}t - E\Big\{ & \frac{m_1}{2}\left[\sin(\omega_{\mathrm{L}}+\omega_r)t + \sin(\omega_{\mathrm{L}}-\omega_r)t\right] \\ & -\frac{m_2}{2}\left[\sin(\omega_{\mathrm{L}}+\omega_z)t + \sin(\omega_{\mathrm{L}}-\omega_z)t\right]\Big\}. \end{aligned} \tag{7.2}$$

The second and third terms correspond to the first sideband caused by the radial and axial secular motions, respectively. When the modulation indexes of m_1, m_2 become larger, including higher order components is necessary in the expansion. For example, $\cos(m_1\cos\omega_r t + m_2\cos\omega_z t)$ in the first term of

Eq. 7.1 is expanded within the second order component as

$$\begin{aligned} E'_{\mathrm{L}} \simeq & E\cos\omega_{\mathrm{L}}t\left[1-\frac{(m_1\cos\omega_r t+m_2\cos\omega_z t)^2}{2}\right] \\ = & \cos\omega_{\mathrm{L}}t\left\{\left[1-\frac{m_1^2}{4}-\frac{m_2^2}{4}\right]-\frac{m_1^2}{4}\cos 2\omega_r t-\frac{m_2^2}{4}\cos 2\omega_z t\right\} \\ & -\frac{m_1 m_2}{4}\left\{\cos\left[\omega_{\mathrm{L}}+(\omega_r+\omega_z)\right]t+\cos\left[\omega_{\mathrm{L}}-(\omega_r+\omega_z)\right]t\right\} \\ & -\frac{m_1 m_2}{4}\left\{\cos\left[\omega_{\mathrm{L}}+(\omega_r-\omega_z)\right]t+\cos\left[\omega_{\mathrm{L}}-(\omega_r-\omega_z)\right]t\right\}. \end{aligned} \tag{7.3}$$

The second and third terms of Eq.7.3 shows the subsidebands of $\omega_r \pm \omega_z$. More precisely, Eq. 7.1 can be described using a Bessel function of the first kind of $J_n(m)$ as

$$E_{\mathrm{L}} = E\sum_{n_1=-\infty}^{\infty}\sum_{n_2=-\infty}^{\infty}\left[J_{n_1}(m_1)J_{n_2}(m_2)\right]\cos\left(\omega_{\mathrm{L}}t+n_1\omega_r t+n_2\omega_z t+\frac{\pi(n_1+n_2)}{2}\right). \tag{7.4}$$

Because the cooling and clock laser beams are colinearly introduced into the trap, the secular motions in the directions, which can be detected using clock laser, were once cooled. The observed spectra indicates a high heating rate after the cooling beam was blocked for spectroscopy of the clock transition to avoid the light shifts. The clock beam colinearly propagated along the cooling beam and was insensitive to the motions perpendicular to the cooling beam. The resolved sideband spectra exhibited the sidebands of considerable intensities generated by not only nonlinear motions but also fundamental secular motions. This indicated that the anharmonicity in the pseudopotential couples the motions perpendicular to the cooling and clock beams with those parallel to them.

7.2 Micromotion minimization in three dimensions

We investigated the resolved-sideband spectra as we further reduced the translational energy of the trapped single ions. Owing to the rotational symmetry of our trap, two degrees of freedom in the radial potential are de-

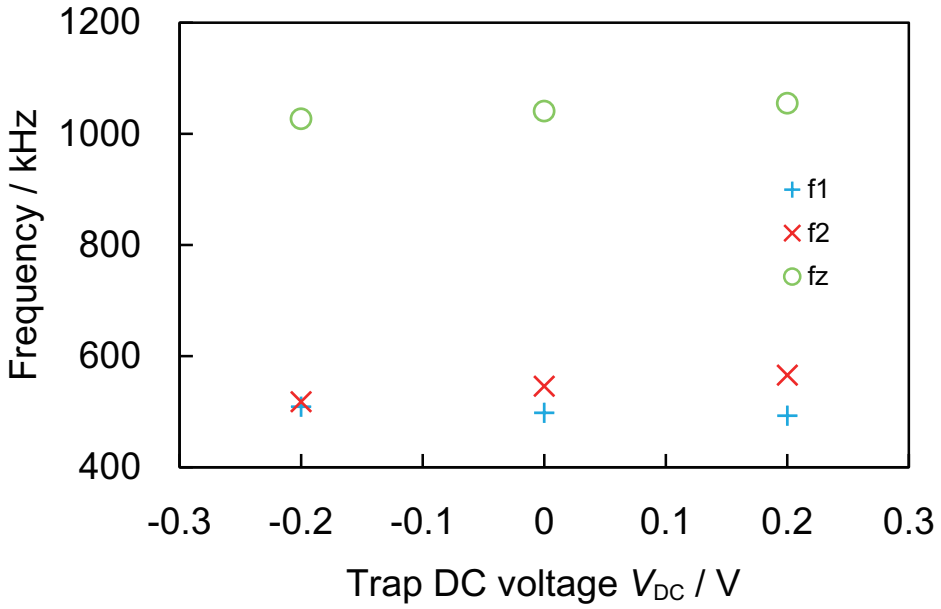

Figure 7.4: Dependence of RF resonance frequencies on V_{DC} superimposed to V_{AC} driving voltage. The plus marks, crosses, and circles show f_1, f_2, f_z, respectively, which are the same as these in Fig. 7.3. We identified that $f_1 = f_r$ and $f_2 = f_z - f_r$ because f_1 and f_z indicated an opposite dependence and that $f_1 + f_2 = f_z$.

generated and the radial secular motion perpendicular to the cooling beam is uncooled [48]. To cool the degenerated radial secular motions and to improve excess micromotion minimization, we introduced the second cooling beam along a different azimuthal angle to the trap axis from that of the first one. We adjusted compensation voltages to eliminate the RF-photon correlation signals detected using both cooling beams to improve excess micromotion minimization. The compensation voltages were adjusted as follows. We set the compensation voltages to the endcap electrode using the first cooling beam as described in Section 4.1.3 and we observed the correlation using the second cooling beam. If we detected a residual correlation using the second cooling beam, we changed the compensation voltage to the endcap electrode slightly, minimized the correlation using the first cooling beam by adjusting the compensation voltages to the compensation electrodes this time, and then observed the correlation using the second cooling beam. We repeated the procedure above until the correlations using both cooling beams were simultaneously minimized.

We show a resolved-sideband spectrum after excess micromotion minimization using the RF-photon correlation detected by two cooling beams in Fig. 7.5; additionally, the RF-photon correlation signals when the spectrum were detected in Fig. 7.6. Although the secular motions in all degrees of freedom were cooled and the excess micromotions along the two cooling beams were simultaneously minimized, we could still observe the structures in the resolved-sideband spectrum.

Even though two cooling beams were used to detect the RF-photon correlation, it was impossible to detect the micromotion along the line that corresponded to the intersection between the two planes perpendicular to the two cooling beams. This excess micromotion is only one component of the residual large translational energy and could be a heating source.

To detect the residual excess micromotion using RF-photon correlation, a third cooling beam in a direction different from those of the two beams is required. Otherwise, other methods that are sensitive to the excess micromotion perpendicular to the two cooling beams are required. We adopted one of the later methods, i.e, the modulation of the trap pseudopotential [18,21]. When the residual stray DC field after the compensation using RF-photon correlation detected using the two cooling beams has a component perpendicular to the two cooling beams, the change in the ion position by the pseudopotential modulation results in a synchronous modulation in the fluorescence intensity, owing to the Gaussian profile of the cooling beam. The principle was shown in Section 2.3.2.

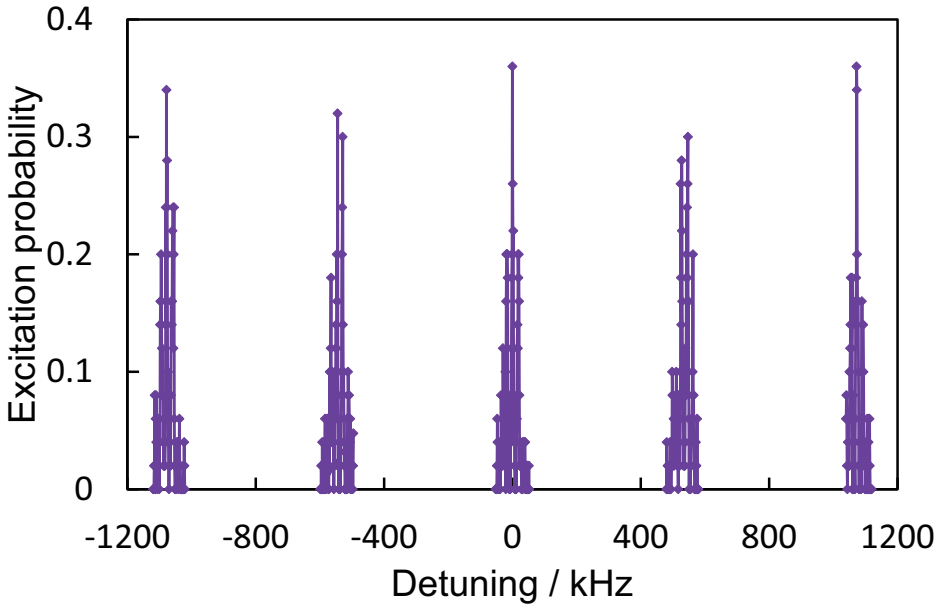

Figure 7.5: Resolved-sideband spectrum of ${}^2S_{1/2}(m_j = -1/2) - {}^2D_{5/2}(m_{j'} = -5/2)$ transition when excess micromotion was minimized by eliminating RF-photon correlation detected using two cooling beams.

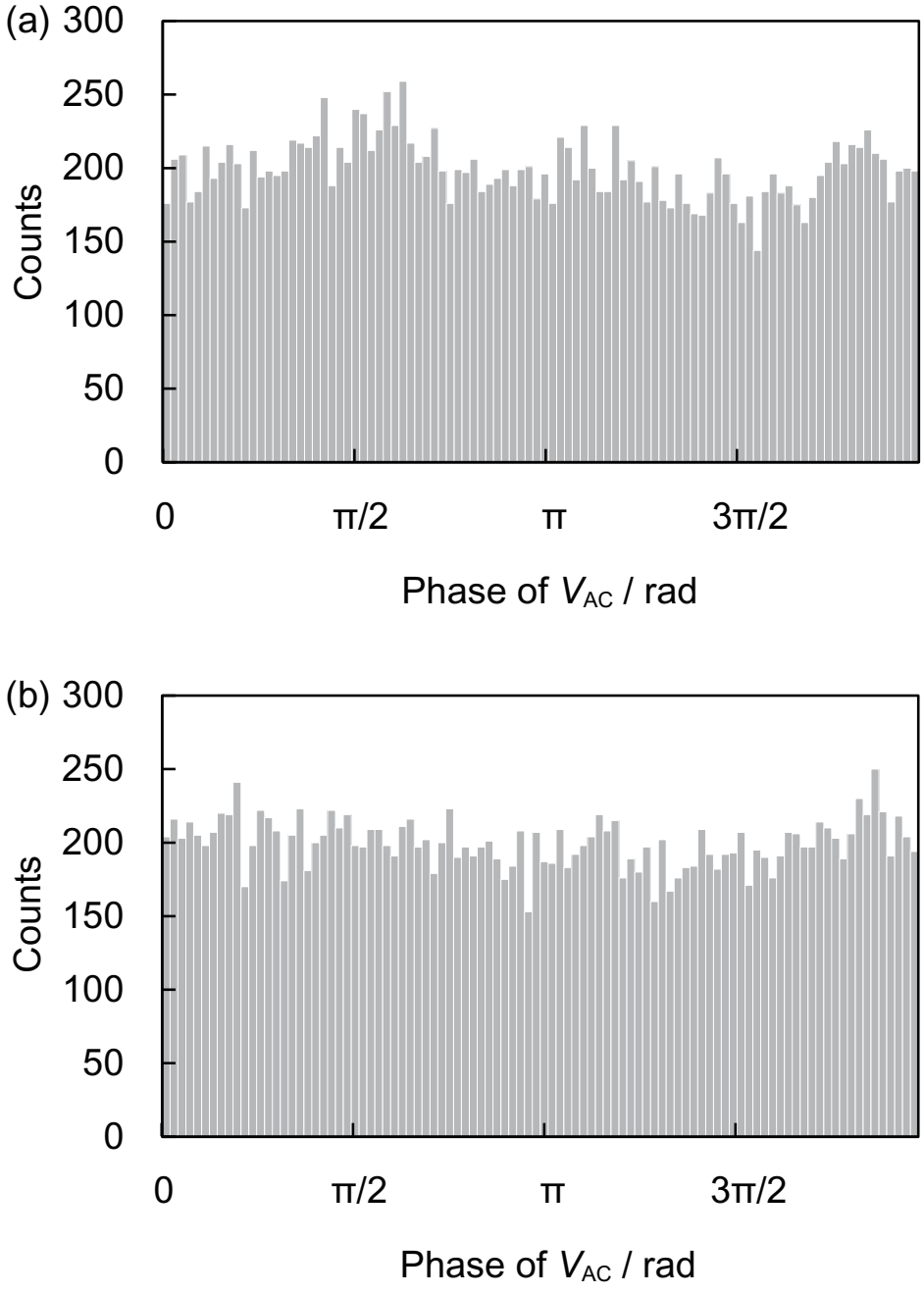

Figure 7.6: RF-photon correlation signals measured using each of two cooling beams when the spectrum shown in Fig. 7.5 was detected. (a): correlation detected using the first cooling beam; (b): using the second cooling beam.

Figure 7.7 shows an example of fluorescence-intensity modulation caused by a slow modulation of V_{AC}. We measured the variation in the fluorescence intensity caused by the modulation of V_{AC} as a function of the voltage applied to one of the pairs of the compensation electrodes (compensation electrodes 1). The results are shown in Fig. 7.8. At each voltage to compensation electrodes 1 at which we measured the fluorescence-intensity modulation shown in Fig. 7.8, we eliminated RF-photon correlation signals detected using the two cooling beams by adjusting the compensation voltages applied to the endcap electrode and the other pair of the compensation electrodes (compensation electrodes 2) before the modulation detection of V_{AC}. These voltages are plotted in Fig. 7.9. The compensation voltages determined from RF-photon correlation detected using the two cooling beams were linearly changed with respect to the voltage applied to compensation electrodes 1. This result shows that the residual stray DC field had a fixed direction to generate the excess micromotion perpendicular to the two cooling beams.

Figure 7.10 shows a resolved-sideband spectrum after we three-dimensionally compensated the stray DC field. Not only the subsideband structures were suppressed, but also the heating rate of the trapped single ion was greatly reduced. When we measured this spectrum, we decreased the clock power to 10 nW to avoid saturation in the carrier spectrum. Below the saturation, we can determine the temperatures of secular motions from the relative intensities of the sidebands to the carrier [52]. The results are 0.9 mK and 4.3 mK for the radial and the axial secular motions, respectively. We do not understand the reason for the difference between the radial and axial temperatures. The radial temperature was slightly higher than the Doppler cooling limit of the cooling transition of 0.47 mK estimated from the lifetime of the $^2P_{1/2}$ state [53]; this is explained by the saturation of the cooling transition [27].

7.3 Discussions

One possible explanation of the observed high heating rate is that the residual displacement of the time-averaged ion position from the trap center would induce the crystal-cloud phase transition. The crystal-cloud phase transition, including a chaotic regime in the case of more than two ions, was extensively investigated in [54, 55]. When we introduce two cooling beams, the secular motions are laser cooled in all degree of freedom. If the residual displacement is large and the single ion is in the cloud regime, however, the residual motion of the excess micromotion is rapidly thermalized to the secular motions and

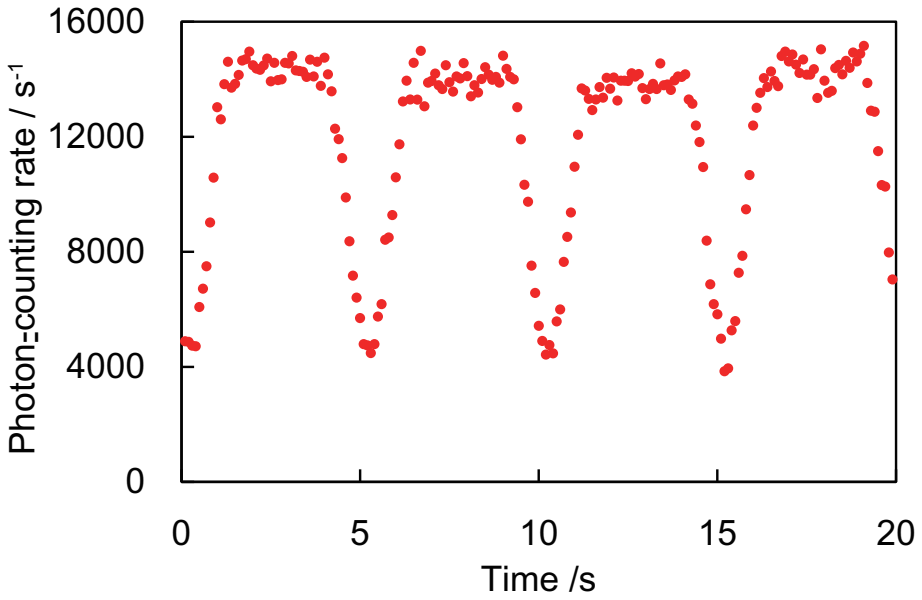

Figure 7.7: Modulation in photon-counting rate of fluorescence intensity by amplitude modulation of V_{AC}. The modulation frequency and the modulation index are 200 mHz and 0.4, respectively.

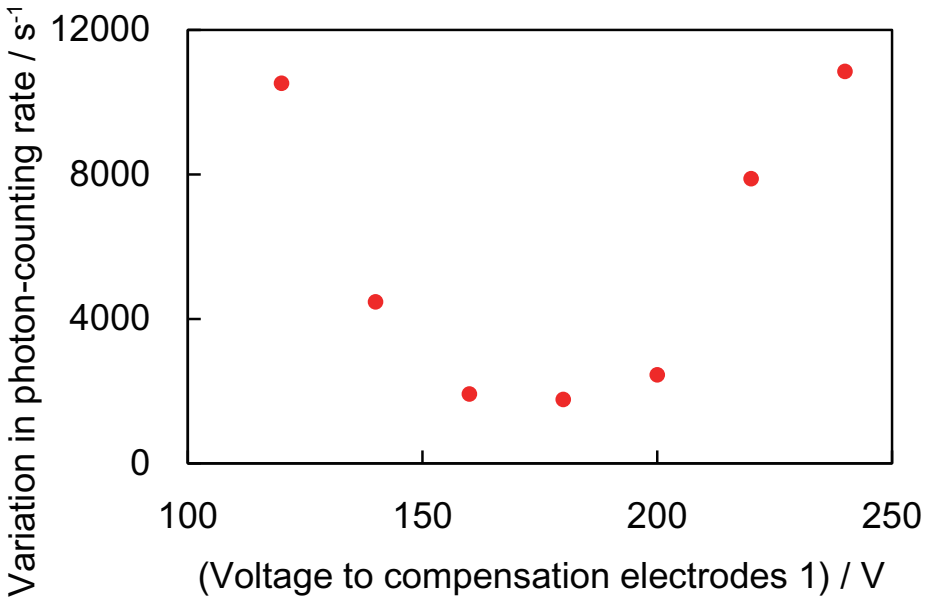

Figure 7.8: Variation in photon-counting rate measured by amplitude modulation of V_{AC} as a function of voltage applied to one of pairs of compensation electrodes, indicated as compensation electrodes 1. The variation means the difference between the maximum and minimum photon-counting rate during the amplitude modulation of V_{AC}; measurement data are shown in Fig. 7.7. Measurement was conducted after we first set the voltage to compensation electrodes 1 and then eliminated RF-photon correlation detected using two cooling beams simultaneously by applying compensation voltages to one of the endcap electrodes and the other pair of the compensation electrodes indicated as compensation electrodes 2 in Fig. 7.9.

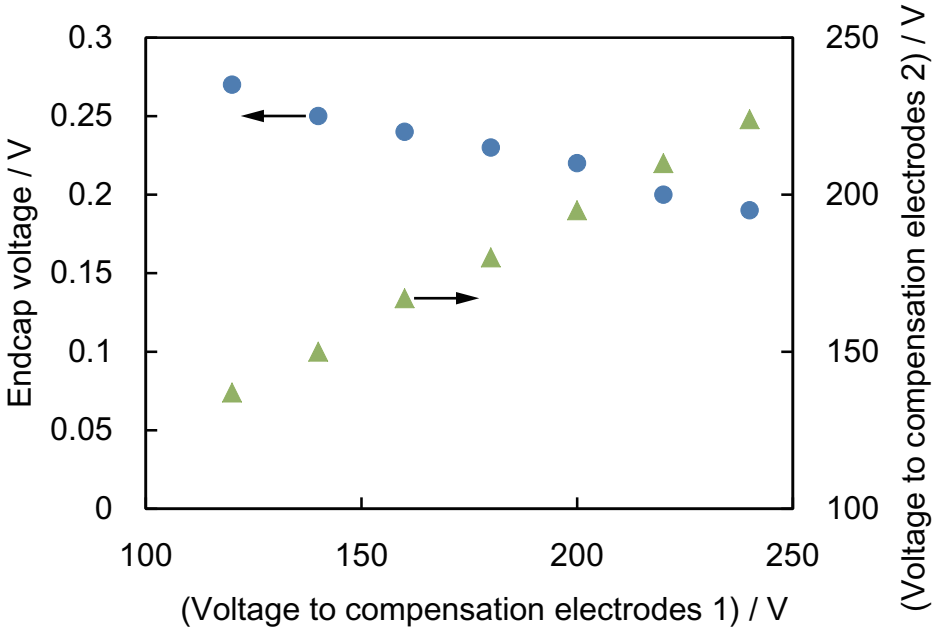

Figure 7.9: Relation among three compensation voltages when the measurement shown in Fig. 7.8 was conducted. At each voltage to compensation electrode 1, the RF-photon correlation detected using two cooling beams were eliminated by applying compensation voltages to one of the endcap electrodes and compensation electrode 2.

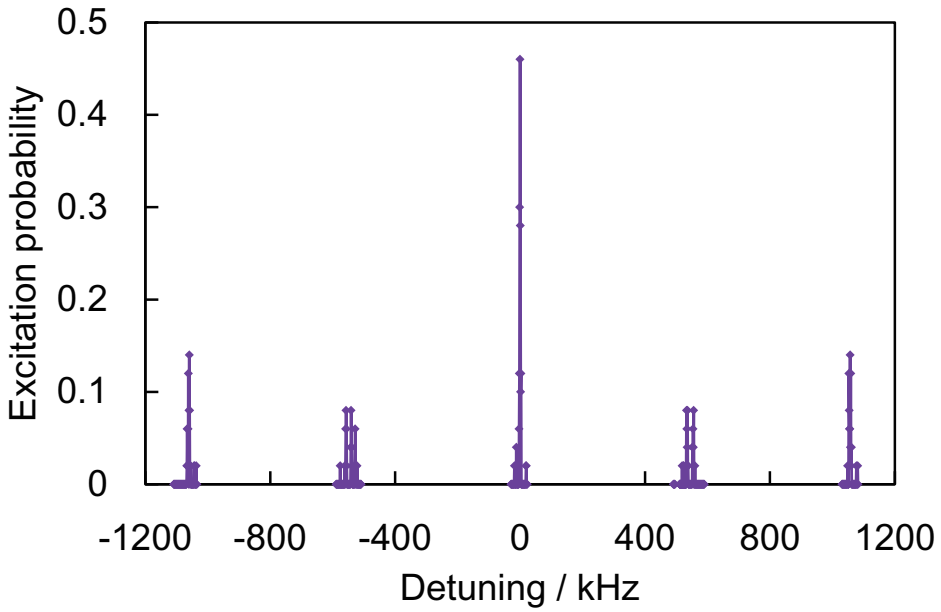

Figure 7.10: Resolved sideband spectrum of ${}^2S_{1/2}(m_j = -1/2) - {}^2D_{5/2}(m_{j'} = -5/2)$ transition when excess micromotions were three-dimensionally minimized. Excess micromotions were minimized by detecting RF-photon correlation using two cooling beams; subsequently, the residual displacement from the trap center was eliminated by detecting it using pseudopotential modulation.

the subsideband structures are generated. Now we succeeded in minimizing the residual displacement and the residual displacement is controllable. This enables us to investigate the proposal above.

As we showed in this chapter, the resolved-sideband spectra are sensitive to the displacement of the time-averaged ion position from the trap center. The subsideband structures in the resolved-sideband spectra could be at least a measure of the residual displacement which causes excess micromotions. In contrast to the RF-photon correlation method, which has a sensitivity to the excess micromotion only along the cooling beam, the resolved-sideband spectra has a sensitivity three-dimensionally, as in the parametric resonance method [30].

It should be noted that the observed subsideband structures shown in Section 7.1 can be explained as nonlinear motions induced by anharmonicity in the trap pseudo potential as shown in Section 7.2. The nonlinear motions and excess micromotions have a common source of enhancement of the time-averaged ion position from the trap center. Therefore, the elimination of a residual displacement through the minimization of excess micromotions would result in the reduction of the subsideband structures. The traps used in this study were fabricated by following the design described in Section 2.1, where C_4 in Eq. 2.11, *i.e.*, the lending term of the anharmonicity was eliminated. However, we cleaned the electrode surface and reassembled the electrodes a few times. This may introduce an anharmonicity to the traps. An evidence of the trap anharmonicity was the detection of the RF electric resonance caused by the secular motion in the radial direction and by the coupled secular motions even when the probe RF field is applied between the endcap electrodes.

The RF-photon correlation method is sensitive to excess micromotions only along the cooling beam. Therefore, the direction of the residual displacement is determined by detecting and minimizing excess micromotions by the RF-photon correlation method using two cooling beams. Combining any other methods that are sensitive to the micromotion perpendicular to the two cooling beams is a convenient scheme to minimize excess micromotions three-dimensionally, instead of introducing a third cooling beam. In particular, for ions trapped in a potential of a cylindrical symmetry such as ours, two cooling beams propagating along different azimuthal angles to the trap axis are inevitable for three-dimensional laser cooling of secular motions. Therefore, the two cooling beams that can be used for the RF-photon correlation method are inevitably introduced.

In the conventional RF trap, the secular frequencies exhibit a relation

that $f_z \sim 2f_r$ according to Eqs. (2.4) and (2.6). Therefore, the frequency $|f_z - 2f_r|$ falls into ~ 0 (In the linear RF trap, $|f_x - f_y| \sim 0$). When this frequency exhibits a small nonzero value and the corresponding subsideband spectra are not resolved from the carrier, the carrier spectrum is broadened and the quality factor as a reference spectrum is degraded, when the intensities of this subsidebands are not sufficiently small. The center frequency of the overlapped carrier spectrum would be shifted when the intensities of the corresponding upper and lower sidebands were different. To check the intensity of the subsideband close to the carrier, it is useful to observe the carrier spectrum as V_{DC} is scanned.

Chapter 8

Conclusions

8.1 Conclusions

In this thesis, we have established systems and techniques for single-ion spectroscopy of two electric quadrupole transitions in Yb^+: the $^2S_{1/2}-{}^2D_{5/2}$ transition in $^{174}Yb^+$ and the $^2S_{1/2}-{}^2D_{3/2}$ transition in $^{171}Yb^+$.

In Chapter 1, we briefly introduce the current status of the optical clock and its applications for the fundamental physics. We emphasis the advantage of Yb^+ ions.

In Chapter 2, we describe the theories and principles required for this study, *i.e.*, the RF trap and laser cooling. The excess micromotion and the nonlinearity in the trap potential, which are essential in this study, are also described. We summarize the properties of Yb^+.

In Chapter 3, we describe the experimental setup developed to conduct this study. We stabilized the frequency of cooling radiation to maintain cooling the ion for a long term. We achieved the stability better than 200 kHz. This value was sufficiently smaller than the linewidth of the $^2S_{1/2}-{}^2P_{1/2}$ cooling transition. To probe the two quadrupole transitions precisely, we linenarrowed the two clock lasers using the resonances of the same high-finesse cavity. We built different precise frequency-scanning methods for the two quadrupole transitions. For a rapid detection of the spectra of the quadrupole transitions in single ions, we developed a system for fast switching lasers with a small dead time between each step of the sequence. One measurement cycle for one clock-laser excitation is completed with a total dead time of approximately 4 ms.

In Chapter 4, we describe laser cooling of $^{174}Yb^+$ and $^{171}Yb^+$ ions. First, we laser cooled $^{174}Yb^+$ ions which have no hyperfine structures. We con-

trolled the number of trapped $^{174}Yb^+$ ions using stepwise increase of fluorescence intensity caused by one-by-one loading. The observed count rate was 15000 $\sim$ 20000 per second for a single ion. It was sufficiently strong to distinguish individual ions. We can load the arbitrary number of trapped ions by blocking the photoionization laser. We canceled the ambient magnetic field at the trap center to apply an magnetic field of arbitrary intensity and direction. This is conducted by observing optical pumping in the magnetic sublevels in the $^2D_{3/2}$ state, which occurs when the $^2D_{3/2}-{}^3D[3/2]_{1/2}$ repumping transition is driven. Second, we laser cooled $^{171}Yb^+$ ions which have hyperfine structures. We investigated the dependence of the fluorescence intensity on the intensity and direction of the magnetic field relative to the polarization of the main cooling laser. For efficient cooling of $^{171}Yb^+$, elimination of optical pumping in the magnetic sublevels in the $^2S_{1/2}(F=0)$ state, which occurs when the $^2S_{1/2}(F=1)-{}^2P_{1/2}(F=0)$ main cooling transition is driven, is required. We found that the magnetic field of a strength grater than 300 μT in the direction of 55 degree from the polarization direction of main cooling laser resulted in the highest fluorescence intensity. We determined the power of the subcooling laser with which the $^2S_{1/2}(F=0)-{}^2P_{1/2}(F=1)$ transition is driven to eliminate pumping to the $^2S_{1/2}(F=0)$ state. We found that 1 nW of the subcooling beam power is sufficient for saturating the transition.

In Chapter 5, we describe single-ion spectroscopy of the $^2S_{1/2}-{}^2D_{5/2}$ transition in $^{174}Yb^+$. The 80 % of Yb^+ in the $^2D_{5/2}$ state decays to the $^2F_{7/2}$ state, which has long lifetime of several years. Detection of the excitation to the $^2D_{5/2}$ state via electron shelving to the $^2F_{7/2}$ state and deexcitation from the $^2F_{7/2}$ state are involved in the computer-controlled spectroscopy sequence. We conducted single-ion spectroscopy of the $\Delta m_j = \pm 2$ transitions selected from ten Zeeman components by applying the magnetic field perpendicular to the polarization of the clock laser. Finally, we resolved the $m_j = -1/2 - m_{j'} = -5/2$ component in $\Delta m_j = -2$ components by applying a magnetic field with a strength of 200 μT. We observed the resolved carrier and sideband spectra of the transition. The width of the carrier spectrum was 20 kHz. This value was limited by an AC magnetic field and the resolution of the frequency scanning of the clock laser.

In Chapter 6, we describe single-ion spectroscopy of the $^2S_{1/2}-{}^2D_{3/2}$ transition in $^{171}Yb^+$. The hyperfine structure of $^{171}Yb^+$ complicates the procedure for the spectroscopy. First, we determined the parameters of spectroscopy for our system using four independent lasers, which were used to drive the cooling and repumping transitions between the hyperfine structures.

The $^2D_{3/2}$ state, the final state of the clock transition, must be decoupled from the laser cooling cycle. We decreased the power of the main repumping beam, with which the $^2D_{3/2}(F=1)-{}^3D[3/2]_{1/2}(F=0)$ transition is driven, to suppress off-resonant excitation of the $^2D_{3/2}(F=2)-{}^3D[3/2]_{1/2}(F=1)$ sub repumping transition by saturation broadening, while the main repumping power has a lower limit to sufficiently repump the $^2D_{3/2}(F=1)$ state. From the observation of spontaneous quantum jumps from the $^2P_{1/2}(F=1)$ state to the $^2D_{3/2}(F=2)$ states, we determine the power range of the main repumping beam to be from 100 μW and 1 mW. Sequentially, we determined the time required for optical pumping to the $^2S_{1/2}(F=0,\, m_F=0)$ state, which is the initial state of spectroscopy. We measured that blocking the sub-cooling beam for 10 ms, with which $^2S_{1/2}(F=0)-{}^2P_{1/2}(F=1)$ transition is driven, was sufficient for the initialization. Subsequently, We conducted single-ion spectroscopy of $^2S_{1/2}(F=0)-{}^2D_{3/2}(F=2)$ transition using the determined parameters.

We resolved all Zeeman components of $\Delta m_F = 0, \pm 1, \pm 2$ transitions by applying a magnetic field of 800 μT and identified the $m_F = 0 - m_{F'} = 0$ magnetic-insensitive transition. We observed the resolved carrier and motional-sideband spectra of the $m_F = 0 - m_{F'} = 0$ transition by frequency sweep of a higher resolution. For further improvement of the resolution, we measured the frequency drift of the clock laser by tracking the center frequency of the carrier spectrum at various time intervals. The measured frequency drift was feedforward compensated to the clock laser during the frequency sweep. We canceled the residual drift, observed even after the feedforward compensation, by taking the carrier spectra twice by reversing the frequency sweep direction of the clock laser We measured a spectral width of the carrier spectrum to be 380 Hz. This value was primarily limited by the clock-laser linewidth.

In Chapter 7, we investigate the resolved motional-sideband spectra of trapped single ions using the $^2S_{1/2}-{}^2D_{5/2}$ transition in $^{174}Yb^+$. The resolved-sideband spectra is important because they are used for evaluation of the energies of the secular motions, which is a large factor of the uncertainty. We found that the resolved-sideband spectra accompanied with subsidebands. We measured the dependence of the RF electric resonance signal caused by the ion motions on the voltages applied for trapping, *i.e*, the amplitude of the AC driving voltage and the DC voltage adjusting the potential depth between the axial and radial directions. From this measurement, we identified the subsidebands with the coupling of the secular motions in the different directions. This is understood that large phase modulations by the secular

motions generated the subsidebands of mixing of the secular frequencies in the different directions. This observation indicates that the single ion was confined out of the Lamb-Dicke region. The subsideband structures were even observed when we laser cooled the secular motions of all degree of freedom by introducing two cooling beams in different directions into the trap. We three-dimensionally minimized excess micromotions by detecting them using RF-photon correlation in two different directions and the pseudopotential modulation. This greatly reduced the subsidebands. We evaluated that the energy of the secular motions were cooled close to the Doppler cooling limit. This observation indicated that the heating rate was increased as the residual displacement of the time-averaged ion position from the trap center, which induced excess micromotions, was larger.

8.2 Prospect

As described above, we have established the method of cooling single Yb^+ ions to near Doppler cooling limit, cooling $^{171}Yb^+$ which has the clock transitions insensitive to the magnetic field, and single-ion spectroscopy of the two electric quadrupole transitions. Owing to the progress on this paper, the realization of the single-ion optical clock is feasible by stabilization of the clock laser frequency to the $^2S_{1/2}(F = 0, m_F = 0) - {}^2D_{3/2}(F' = 2, m_{F'} = 0)$ transition and evaluation of the uncertainty in various frequency shifts. Similarly, we aim at realization of optical clocks based on the $^2S_{1/2}(F = 0, m_F = 0) - {}^2D_{5/2}(F' = 2, m_{F'} = 0)$, $^2S_{1/2}(F = 0, m_F = 0) - {}^2F_{7/2}(F' = 3, m_{F'} = 0)$ transitions. The frequency ratio measurements among the three optical clocks enable us to contribute the redefinition of the second, and search for a temporal variation of the fine structure constant α with investigating other effects which causes temporal variations.

Bibliography

[1] S. M. Brewer, J.-S. Chen, E. R. Hankin, E. R. Clements, C.-W. Chou, D. J. Wineland, D. B. Hume, and D. R. Leibrandt. $^{27}Al^{+}$ quantum-logic clock with a systematic uncertainty below 10^{-18}. *Physical Review Letters*, 123(3):033201, 2019.

[2] B. J. Bloom, T. L. Nicholson, J. R. Williams, S. L. Campbell, M. Bishof, X. Zhang, W. Zhang, S. L. Bromley, and J. Ye. An optical lattice clock with accuracy and stability at the 10^{-18} level. *Nature*, 506(7486):71–75, February 2014.

[3] V. V. Flambaum, A. J. Geddes, and A. V. Viatkina. Isotope shift, non-linearity of King plots and the search for new particles. *Physical Review A*, 97(3):032510, March 2018.

[4] N. Huntemann, C. Sanner, B. Lipphardt, Chr. Tamm, and E. Peik. Single-ion atomic clock with 3×10^{-18} systematic uncertainty. *Physical review letters*, 116(6):063001, 2016.

[5] R. Wynands and S. Weyers. Atomic fountain clocks. *Metrologia*, 42(3):S64–S79, June 2005.

[6] T. L. Nicholson, S. L. Campbell, R. B. Hutson, G. E. Marti, B. J. Bloom, R. L. McNally, W. Zhang, M. D. Barrett, M. S. Safronova, G. F. Strouse, W. L. Tew, and J. Ye. Systematic evaluation of an atomic clock at 2×10^{-18} total uncertainty. *Nature Communications*, 6(1):6896, November 2015.

[7] I. Ushijima, M. Takamoto, M. Das, T. Ohkubo, and H. Katori. Cryogenic optical lattice clocks. *Nature Photonics*, 9(3):185–189, March 2015.

[8] A. D. Ludlow, M. M. Boyd, J. Ye, E. Peik, and P. O. Schmidt. Optical atomic clocks. *Reviews of Modern Physics*, 87(2):637–701, June 2015.

[9] H. G. Dehmelt. Monoion oscillator as potential ultimate laser frequency standard. *IEEE Transactions on Instrumentation and Measurement*, IM-31(2):83–87, June 1982.

[10] J.-P. Uzan. The fundamental constants and their variation: Observational and theoretical status. *Reviews of Modern Physics*, 75(2):403–455, April 2003.

[11] T. Rosenband, D. B. Hume, P. O. Schmidt, C. W. Chou, A. Brusch, L. Lorini, W. H. Oskay, R. E. Drullinger, T. M. Fortier, J. E. Stalnaker, S. A. Diddams, W. C. Swann, N. R. Newbury, W. M. Itano, D. J. Wineland, and J. C. Bergquist. Frequency Ratio of Al^+ and Hg^+ Single-Ion Optical Clocks; Metrology at the 17th Decimal Place. *Science*, 319(5871):1808, 2008.

[12] E. Peik, B. Lipphardt, H. Schnatz, T. Schneider, Chr. Tamm, and S. G. Karshenboim. Limit on the Present Temporal Variation of the Fine Structure Constant. *Physical Review Letters*, 93(17):170801, October 2004.

[13] V. V. Flambaum and V. A. Dzuba. Search for variation of the fundamental constants in atomic, molecular and nuclear spectra. *Canadian Journal of Physics*, 87(1):25–33, January 2009.

[14] M. Roberts, P. Taylor, G. P. Barwood, P. Gill, H. A. Klein, and W. R. C. Rowley. Observation of an electric octupole transition in a single ion. *Physical Review Letters*, 78:1876–1879, March 1997.

[15] Chr. Tamm, N. Huntemann, B. Lipphardt, V. Gerginov, N. Nemitz, M. Kazda, S. Weyers, and E. Peik. Cs-based optical frequency measurement using cross-linked optical and microwave oscillators. *Physical Review A*, 89(2):023820, February 2014.

[16] P. Dubé, A. A. Madej, M. Tibbo, and J. E. Bernard. High-accuracy measurement of the differential scalar polarizability of a $^{88}Sr^+$ clock using the time-dilation effect. *Physical Review Letters*, 112:173002, April 2014.

[17] D. Engelke and Chr. Tamm. Dark times in the resonance fluorescence of trapped ^{171}Yb ions caused by spontaneous quantum jumps to the $^2D_{3/2}(F = 2)$ state. *Europhysics Letters (EPL)*, 33(5):347–352, February 1996.

[18] Chr. Tamm, D. Engelke, and V. Bühner. Spectroscopy of the electric-quadrupole transition ${}^2S_{1/2}(F = 0)-{}^2D_{3/2}(F = 2)$ in trapped ${}^{171}\mathrm{Yb}^+$. *Physical Review A*, 61:053405, April 2000.

[19] M. Roberts, P. Taylor, S. V. Gateva-Kostova, R. B. M. Clarke, W. R. C. Rowley, and P. Gill. Measurement of the ${}^2S_{1/2}-{}^2D_{5/2}$ clock transition in a single ${}^{171}\mathrm{Yb}^+$ ion. *Physical Review A*, 60(4):2867–2872, October 1999.

[20] V. A. Dzuba, V. V. Flambaum, and M. V. Marchenko. Relativistic effects in Sr, Dy, Yb II, and Yb III and search for variation of the fine-structure constant. *Physical Review A*, 68(2):022506, August 2003.

[21] D. J. Berkeland, J. D. Miller, J. C. Bergquist, W. M. Itano, and D. J. Wineland. Minimization of ion micromotion in a paul trap. *Journal of Applied Physics*, 83(10):5025–5033, May 1998.

[22] W. Paul. Electromagnetic traps for charged and neutral particles. *Reviews of Modern Physics*, 62(3):531–540, July 1990.

[23] Lowell S. Brown and Gerald Gabrielse. Geonium theory: Physics of a single electron or ion in a penning trap. *Reviews of Modern Physics*, 58:233–311, Jan 1986.

[24] K. Sugiyama and J. Yoda. Anharmonic oscillation of ions trapped in a rf trap with light buffer gas. *Applied Physics B*, 51:146–152, August 1990.

[25] F. Vedel and M. Vedel. Nonlinear effects in the detection of stored ions. *Physical Review A*, 41(5):2348–2351, March 1990.

[26] T. W. Hänsch and A. L. Schawlow. Cooling of gases by laser radiation. *Optics Communications*, 13(1):68–69, January 1975.

[27] D. Leibfried, R. Blatt, C. Monroe, and D. Wineland. Quantum dynamics of single trapped ions. *Rev. Mod. Phys.*, 75:281–324, Mar 2003.

[28] R. Blümel, C. Kappler, W. Quint, and H. Walther. Chaos and order of laser-cooled ions in a paul trap. *Phys. Rev. A*, 40:808–823, Jul 1989.

[29] J. Keller, H. L. Partner, T. Burgermeister, and T. E. Mehlstäubler. Precise determination of micromotion for trapped-ion optical clocks. *Journal of Applied Physics*, 118(10):104501, September 2015.

[30] Y. Ibaraki, U. Tanaka, and S. Urabe. Detection of parametric resonance of trapped ions for micromotion compensation. *Applied Physics B*, 105(2):219–223, November 2011.

[31] E. H. Pinnington, R. W. Berends, and Q. Ji. Beam-laser lifetime measurements of Yb II energy levels. *Physical Review A*, 50(3):2758–2760, September 1994.

[32] Ch. Gerz, J. Roths, F. Vedel, and G. Werth. Lifetime and collisional depopulation of the metastable $5D_{3/2}$-state of Yb^+. *Zeitschrift für Physik D Atoms, Molecules and Clusters*, 8(3):235–237, September 1988.

[33] P. Taylor, M. Roberts, S. V. Gateva-Kostova, R. B. M. Clarke, G. P. Barwood, W. R. C. Rowley, and P. Gill. Investigation of the $^2S_{1/2}-^2D_{5/2}$ clock transition in a single ytterbium ion. *Physical Review A*, 56(4):2699–2704, October 1997.

[34] R. W. Berends, E. H. Pinnington, B. Guo, and Q. Ji. Beam-laser lifetime measurements for four resonance levels of Yb II. *Journal of Physics B: Atomic, Molecular and Optical Physics*, 26(20):L701–L704, October 1993.

[35] A. S. Bell, P. Gill, H. A. Klein, A. P. Levick, Chr. Tamm, and D. Schnier. Laser cooling of trapped ytterbium ions using a four-level optical-excitation scheme. *Physical Review A*, 44(1):R20–R23, July 1991.

[36] N. Yu and L. Maleki. Lifetime measurements of the $4f^{14}5d$ metastable states in single ytterbium ions. *Physical Review A*, 61(2):022507, January 2000.

[37] S. Olmschenk, K. C. Younge, D. L. Moehring, D. N. Matsukevich, P. Maunz, and C. Monroe. Manipulation and detection of a trapped Yb^+ hyperfine qubit. *Physical Review A*, 76(5):052314, November 2007.

[38] S. A. King, R. M. Godun, S. A. Webster, H. S. Margolis, L. A. M. Johnson, K. Szymaniec, P. E. G. Baird, and P. Gill. Absolute frequency measurement of the $^2S_{1/2}-{}^2F_{7/2}$ electric octupole transition in a single ion of $^{171}Yb^+$ with 10^{-15} fractional uncertainty. *New Journal of Physics*, 14(1):013045, January 2012.

[39] P. T. H. Fisk, M. A. Lawn, and C. Coles. Laser cooling of $^{171}Yb^+$ ions in a linear paul trap. *Applied Physics B Photophysics and Laser Chemistry*, 57(4):287–291, October 1993.

[40] K. Sugiyama, S. Kawajiri, N. Yabu, K. Matsumoto, and M. Kitano. Sum-frequency mixing of radiation from two extended-cavity laser diodes using a doubly resonant external cavity for laser cooling of trapped ytterbium ions. *Applied Optics*, 49(29):5510, October 2010.

[41] E. W. Streed, T. J. Weinhold, and D. Kielpinski. Frequency stabilization of an ultraviolet laser to ions in a discharge. *Applied Physics Letters*, 93(7):071103, August 2008.

[42] K. Sugiyama, K. Sasaki, A. Wakita, and J. Yoda. A laser-diode spectrometer for the $^2S_{1/2}-^2D_{5/2}$ transition of single laser-cooled trapped Yb^+. In *1998 Conference on Precision Electromagnetic Measurements Digest (Cat. No.98CH36254)*, pages 408–409, July 1998.

[43] R. W. P. Drever, J. L. Hall, F. V. Kowalski, J. Hough, G. M. Ford, A. J. Munley, and H. Ward. Laser phase and frequency stabilization using an optical resonator. *Applied Physics B Photophysics and Laser Chemistry*, 31(2):97–105, June 1983.

[44] Y. Onoda, K. Sugiyama, M. Ikeda, and M. Kitano. Loading rate of Yb^+ loaded through photoionization in radiofrequency ion trap. *Applied Physics B*, 105(4):729–740, December 2011.

[45] E. C. Beaty. Simple electrodes for quadrupole ion traps. *Journal of Applied Physics*, 61(6):2118–2122, 1987.

[46] Chr. Balzer, A. Braun, T. Hannemann, Chr. Paape, M. Ettler, W. Neuhauser, and Chr. Wunderlich. Electrodynamically trapped Yb^+ ions for quantum information processing. *Physical Review A*, 73(4):041407, April 2006.

[47] S. Ejtemaee, R. Thomas, and P. C. Haljan. Optimization of Yb^+ fluorescence and hyperfine-qubit detection. *Physical Review A*, 82(6):063419, December 2010.

[48] D. J. Wineland and Wayne M. Itano. Laser cooling of atoms. *Physical Review A*, 20(4):1521–1540, October 1979.

[49] J. C. Bergquist, W. M. Itano, and D. J. Wineland. Recoilless optical absorption and Doppler sidebands of a single trapped ion. *Physical Review A*, 36(1):428–430, July 1987.

[50] D. J. Berkeland and M. G. Boshier. Destabilization of dark states and optical spectroscopy in Zeeman-degenerate atomic systems. *Physical Review A*, 65(3):033413, February 2002.

[51] S. Stenholm. The semiclassical theory of laser cooling. *Reviews of Modern Physics*, 58(3):699–739, July 1986.

[52] S. Urabe, M. Watanabe, H. Imajo, K. Hayasaka, U. Tanaka, and R. Ohmukai. Observation of Doppler sidebands of a laser-cooled Ca^+ ion by using a low-temperature-operated laser diode. *Applied Physics B*, 67:223–227, Aug 1998.

[53] S. Olmschenk, D. Hayes, D. N. Matsukevich, P. Maunz, D. L. Moehring, K. C. Younge, and C. Monroe. Measurement of the lifetime of the $6p\ ^2P^o_{1/2}$ level of Yb^+. *Physical Review A*, 80:022502, August 2009.

[54] R. Blümel, C. Kappler, W. Quint, and H. Walther. Chaos and order of laser-cooled ions in a Paul trap. *Physical Review A*, 40(2):808–823, July 1989.

[55] R. Blümel, J. M. Chen, E. Peik, W. Quint, W. Schleich, Y. R. Shen, and H. Walther. Phase transitions of stored laser-cooled ions. *Nature*, 334(6180):309–313, 1988.

List of Publications

A Full Length Papers with Review

1. Y. Imai, T. Nishi, M. Nishizaki1, S. Kawajiri1, Y. Muroki1, R. Ikuta, K. Matsumoto, M. Kitano, and K. Sugiyama,
"Single-ion spectroscopy system for the $^2S_{1/2}(F = 0)$-$^2D_{3/2}(F = 2)$ transition in $^{171}Yb^+$,"
Radio Science, **51**, 1385-1395 (2016)

B Conference Proceedings

1. Y. Imai, K. Sugiyama, K. Matsumoto and M. Kitano,
"Single-ion spectroscopy of the $^2S_{1/2}$-$^2D_{5/2}$ clock transition in $^{174}Yb^+$ stored in an rf trap towards search for temporal variation of the fine structure constant,"
in *Proceeding of the 5th International Workshop on Fundamental Physics Using Atoms 2011*, Okayama, Japan, Oct., pp.99-102

2. Y. Imai, K. Sugiyama, T. Nishi, S. Higashitani, T. Momiyama, and M. Kitano,
"Single-ion spectroscopy of the clock transitions in Yb^+,"
in *Proceeding of the 7th International Workshop on Fundamental Physics Using Atoms 2014*, Tokyo, Japan, Mar., pp.104-107

C International Conferences with Review

1. Y. Imai, K. Sugiyama, T. Nishi, S. Higashitani, T. Momiyama, and M. Kitano
"Single-ion spectroscopy of the $^2S_{1/2}$-$^2D_{5/2}$ clock transitions in Yb^+

towards search for temporal variation of the fine structure constant"
The 12th Asia Pacific Physics Conference, Tokyo, Japan, Jul.(2013)

2. Y. Imai, K. Sugiyama, T. Nishi, S. Higashitani, T. Momiyama, and M. Kitano
"Single-ion spectroscopy of the quadrupole transitions in Yb^+ towards search for temporal variation of the fine structure constant"
IonTech2, Paris, France, Oct. (2013)

3. Y. Imai, K. Sugiyama, S. Higashitani, and M. Kitano
"Spectroscopy of the $^2S_{1/2}$-$^2D_{3/2}$ transition in single $^{171}Yb^+$ towards search for temporal variation of the fine structure constant"
3rd European Conference on Trapped Ions, Mainz, Germany, Sep. (2014)

4. Y. Imai, K. Sugiyama, and M. Kitano
"Observation of the magnetic-insensitive clock transition in the $^2S_{1/2}(F = 0)$-$^2D_{3/2}(F = 2)$ transitions in single $^{171}Yb^+$"
URSI-Japan Radio Science Meeting, Tokyo, Japan, Sep. (2015)

5. Y. Imai, K. Sugiyama, R. Irie, and M. Kitano
"Single-ion spectroscopy of two quadrupole transitions in ytterbium ions towards search for temporal variation of the fine structure constant"
The 25th International Conference on Atomic Physics, Seoul, Korea, Jul. (2016)